

Article

The Influence of Shear-Thinning Characteristics on Multiphase Pump Vortex Structure Evolution, Pressure Fluctuation, and Gas-Solid Distribution

Long Chen ^{1,*}, Yingxin Yang ¹, Cancan Peng ² , Xiaodong Zhang ¹ and Yan Gong ¹ 

¹ Institution of Mechanical and Electrical Engineering, Southwest Petroleum University, Chengdu 610500, China; yangyx36@163.com (Y.Y.); zxd123420@126.com (X.Z.); gongyan0101@163.com (Y.G.)

² China National Petroleum Corporation Chuanqing Drilling Engineering Co., Ltd. Downhole Service Company, Guanghan 610052, China; pengcc_cd@126.com

* Correspondence: 202111000084@stu.swpu.edu.cn

Abstract: In the current landscape of natural gas hydrate extraction, the lifting pump assumes a pivotal role as the essential equipment for conveying subsea fluidized hydrate slurry to the wellhead. The inherent shear-thinning characteristics of natural gas hydrate slurry, compounded by the complex multiphase flow conditions of the “gas-liquid-solid” system, present significant challenges to the operational efficiency and stability of the lifting pump. Consequently, this study adopts a hybrid approach, combining experimental and numerical simulations, to comparatively investigate the impact of non-Newtonian and viscous Newtonian fluids on the hydraulic performance, vortex structure evolution, and induced pressure fluctuations in a multiphase pump. Concurrently, a comparative analysis is conducted on the influence of these two fluid types on the distribution patterns of the “gas-solid” two-phase system. The research findings indicate that the apparent viscosity variations are more pronounced in the diffuser region compared to the impeller region. Under non-Newtonian fluid conditions, two separation vortices emerge at the trailing edge of the diffuser, as opposed to a single separation vortex in the viscous Newtonian fluid, with the latter exhibiting a smaller vortex structure scale. Moreover, the shear-thinning characteristics intensify the interaction between the separated vortex and the mainstream, resulting in an exacerbation of pressure fluctuations. In contrast to the viscous Newtonian fluid, the rotor–stator interaction and shear-thinning characteristics play a predominant role in pressure fluctuations, with shear-thinning attributes giving rise to low-frequency pressure fluctuations. Additionally, shear-thinning characteristics significantly influence the distribution behavior of the gas-solid two-phase flow.

Keywords: shear-thinning property; multiphase pump; vortex evolution; pressure fluctuation; non-Newtonian fluid



Citation: Chen, L.; Yang, Y.; Peng, C.; Zhang, X.; Gong, Y. The Influence of Shear-Thinning Characteristics on Multiphase Pump Vortex Structure Evolution, Pressure Fluctuation, and Gas-Solid Distribution. *Processes* **2024**, *12*, 284. <https://doi.org/10.3390/pr12020284>

Academic Editor: Blaž Likozar

Received: 8 December 2023

Revised: 18 January 2024

Accepted: 23 January 2024

Published: 27 January 2024



Copyright: © 2024 by the authors. Licensee MDPI, Basel, Switzerland. This article is an open access article distributed under the terms and conditions of the Creative Commons Attribution (CC BY) license (<https://creativecommons.org/licenses/by/4.0/>).

1. Introduction

At present, global economic development cannot be separated from the supply of energy, in the development of conventional energy such as coal, oil, etc., due to its limited reserves and more serious harm to the environment. Nowadays, there is a growing demand for non-conventional clean energy in countries all over the world. Among the non-conventional clean energy sources, natural gas hydrate is becoming an important clean energy source in the future because of its high energy density, cleanliness, abundant resources, and wide distribution [1,2]. According to cutting-edge lookup and exploration of proper deposits, natural gas hydrates are usually discovered in conjunction with free water/free gas in nature. Based on the storage conditions of hydrates, free water (sea), and free natural gas under different coexistence scenarios, natural gas hydrate resources can be greatly labeled into three types. The first category pertains to hydrate sediment layers situated above two-phase flow zones, involving a combination of seawater and natural

gas. In such reservoirs, the saturation of hydrate distribution significantly impacts the pore space, leading to a diminished effective permeability of hydrate sediments. Consequently, these reservoirs are deemed the most conducive for hydrate development. The second category encompasses hydrates overlaying areas with flowing water, while the third category involves hydrate reservoirs that extend throughout the entire geological formation [3]. In contrast to the first type of reservoir, the second and third categories face significant challenges, including potential safety concerns such as reservoir collapse, seabed landslides, and geological fractures. Moreover, economic viability poses an additional hurdle. As a result, these latter reservoir types have not yet been considered for development and extraction targets [4].

To facilitate the development of shallow, weakly cemented seabed gas hydrates, a development method termed solid-state fluidization mining was proposed by Zhou Shouwei and his colleagues [5]. This methodology capitalizes on the inherent stability of natural gas hydrates under seabed temperature and pressure conditions. It employs a solid-state mining method wherein the sediment from natural gas hydrate reservoirs undergoes primary and secondary crushing to reduce it to fine particles. Subsequently, a scientifically devised process is applied to fluidize these crushed hydrate particles by integrating them with seawater. Following pre-separation to eliminate sediment, a closed pipeline is utilized for the transportation of the hydrate slurry to an offshore platform for further processing and treatment. In order to solve the problem of pumping multiphase fluids containing seabed hydrate slurry to the drilling platform, we developed a lifting multiphase pump that can effectively adapt to the mixing of “gas-liquid-solid” three-phase transportation, and its structure is shown in Figure 1. The pump utilizes high-pressure seawater to drive the rotation of the turbine section to provide power for the lifting pump, so as to pump multiphase fluids to the sea level. Numerous experimental studies have pointed out that hydrate slurries extracted by introducing seawater and clays from seabed sediments exhibit non-Newtonian fluid properties. Unlike the pure viscosity of Newtonian fluids, hydrate slurries exhibit special properties of non-Newtonian fluid flow such as shear thinning, yield stress, and viscoelasticity. Given the cost and safety factors, many researchers usually choose water as the test medium when evaluating the performance of multiphase pumps, and thus the studies on using non-Newtonian fluids as the test medium are relatively limited.

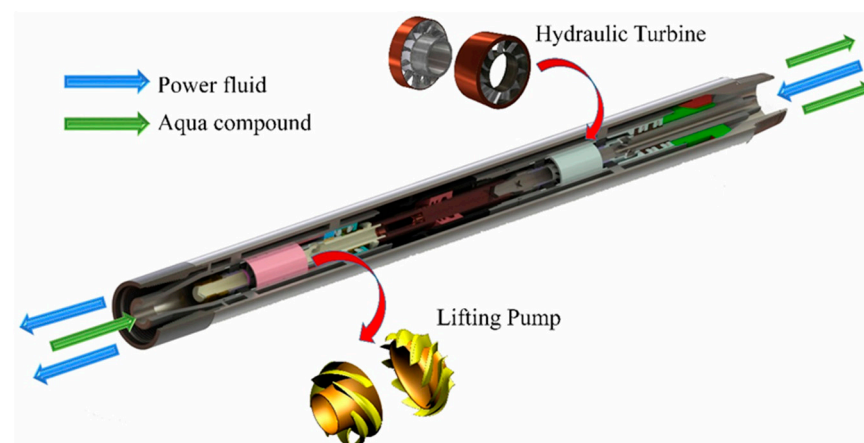


Figure 1. Schematic diagram of the structure of the lifting multiphase pump system.

During the operation of a multiphase pump, pressure increment, flow rate, vortex structure, and pressure fluctuations are crucial factors influencing the safe and efficient operation of the pump [6,7]. With the advancement of technology, some advanced measurement devices such as high-speed cameras [8], laser Doppler velocimeters [9], and particle image velocimetry systems [10] have been employed to study the flow phenomena inside pumps. However, owing to factors like the complexity of pump blade geometry,

experimental costs, and the intricate nature of fluid flow, obtaining precise information about the flow behavior within the pump remains challenging. Currently, computational fluid dynamics (CFD) techniques are increasingly applied in the research of fluid machinery. Liu and Tan et al. [11] conducted a study on the pressure pulsation intensity and vortex characteristics of mixed-flow pumps with blade tip clearances. The results indicated that flow rate significantly affects the structure and trajectory of tip-leakage vortices, and there is an important relationship between the pressure fluctuations near the blade tip clearance and the evolution of vortex structures. Zhang et al. [12], through investigating the relationship between blade tip clearance size and pressure fluctuations, found that within a certain range, the size of the tip clearance has a relatively small impact on pressure fluctuations, but when the clearance value reaches 1 mm, there is a noticeable increase in pressure fluctuations in the impeller inlet section. Kan et al. [13] explored water flow in a rotating axial pump via large-eddy simulation, employing a sharp-interface level-set immersed boundary method. Turbulence statistics reveal distinct flow characteristics under varied flow-rate conditions, emphasizing the impact of tip leakage flow and flow separation. Kan et al. [14] investigated axial-flow pump safety, focusing on tip leakage flow (TLF), via numerical simulations. The study examined TLV characteristics, energy loss, and spatial evolution under varying tip clearances and operating conditions. Sonawat et al. [15] and Tan et al. [16] proposed optimizing the blade tip clearance size of axial-flow pumps to suppress pressure fluctuations, thereby enhancing the hydraulic performance of pumps during operational conditions. These studies were conducted under the assumption of Newtonian fluid behavior. However, in certain special conditions, such as when handling high-viscosity slurries or oil-water mixtures, the conveying medium can exhibit non-Newtonian characteristics due to shear-thinning effects. Liu et al. [17] investigated the differences in multiphase pump flow fields at different viscosities and found that as viscosity increases, the pump head and efficiency gradually decrease. They used partial differential equations to reveal the impact of viscosity and established a model to predict the effect on flow rate. Valdés et al. [18] studied the performance of centrifugal pumps under two conditions: shear-thinning non-Newtonian fluid and Newtonian fluid. They found that the performance deterioration can be explained by significant changes in viscosity. Zhu et al. [19] through a combination of experiments and numerical simulations, studied the influence of viscosity on pump performance and found that in high-viscosity fluid media, increased wall shear stress leads to a sudden drop in pressure within the pump channel. Ebrahimi et al. [20] explored the impact of viscosity variations on vortex structures and noted that viscosity changes directly affect shear stress and flow boundary layers, subsequently affecting flow structures like vortices and secondary flows. Li et al. [21] in their research on centrifugal pumps transporting high-viscosity fluids, observed a sudden rise in head and attributed this phenomenon to the shear-thinning effect. They introduced standard $k-\epsilon$ turbulence models and non-equilibrium wall functions into Reynolds-averaged Navier–Stokes (RANS) equations to explain the sudden head change effect caused by shear thinning. Numerous studies suggest that compared to Newtonian fluids, the shear-thinning characteristics of non-Newtonian fluids lead to significant changes in pump performance and internal flow fields (such as gap leakage, flow separation vortices, turbulence energy) and the distribution of different phases during multiphase transport [22].

In summary, the internal flow characteristics of multiphase pumps in non-Newtonian fluids have been extensively studied by scholars, with a primary focus on axial-flow pumps and centrifugal pumps. The principal objective of this paper is to investigate the vortex evolution, pressure fluctuation, and other internal flow characteristics of multiphase pumps in transporting non-Newtonian fluids, which are closer to the actual working conditions, by adopting the simulation method of non-stationary transient, in order to better explain the differences between multiphase pumps in transporting non-Newtonian and viscous Newtonian fluids and to better guide the optimal design of multiphase pumps to improve its performance. The fundamental structure of this paper unfolds in the following sequence: firstly, the reliability of numerical methods is substantiated through experimental validation;

secondly, the presentation covers the characteristics of apparent viscosity and shear rate variation; following that, a systematic evaluation delves into the evolutionary process of the expansion chamber trailing edge separation vortex; and finally, the intricate relationship between vortex evolution and pressure fluctuations is unveiled.

2. Problem Set

2.1. Physical Model

In order to cope with the special performance requirements of “gas-liquid-solid” three-phase mixing required for natural gas hydrate extraction, this study adopts a self-designed multiphase pump. The essential design parameters of this multiphase pump are as follows: design flow rate of 120 m³/h, head of 20 m, and design speed of 3500 rpm. The detailed configurations of the impeller and diffuser are visually elucidated in Figure 2.



Figure 2. Multiphase pump: (a) impeller; (b) diffuser.

The 3D model of the impeller and diffuser is shown in Figure 3. The single-stage multiphase pump model is primarily composed of an impeller, diffuser, and inlet and outlet sections. To ensure the stability of fluid flow in the inlet and outlet sections before entering the impeller region and eliminate errors introduced by flow instability, the lengths of the inlet and outlet sections are set to five times the diameter of the pipe segment.

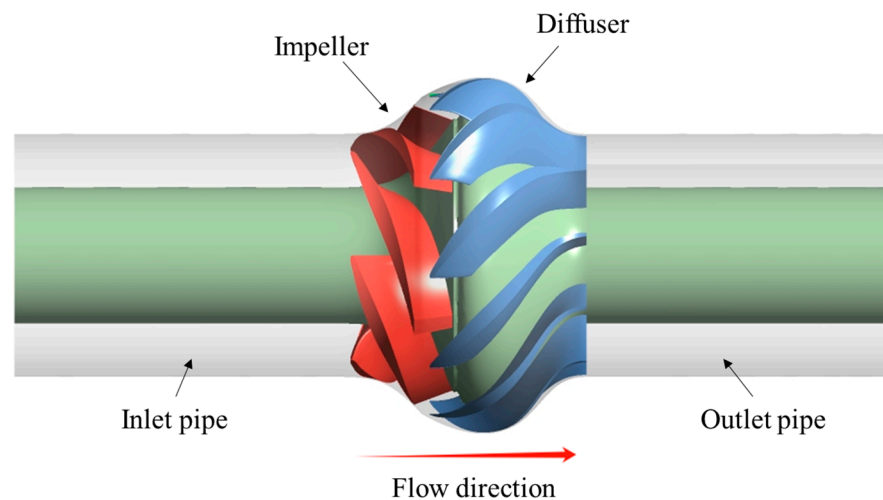


Figure 3. Schematic of the physical model of a multiphase pump.

2.2. Parameterization of Operating Conditions

Drawing upon the fundamental parameters established for a field trial encompassing the solid-state fluidization and jet fragmentation of marine natural gas hydrates in China, this paper defines the operational parameters for the designed multiphase pump as a water depth of 1310 m and a pressure of 13.7 MPa, within a marine environment characterized by silty sand.

In this study, natural gas is selected as the gaseous medium. It is well established that under STP (standard temperature and pressure) conditions, natural gas primarily comprises methane, exhibiting a density of 0.7174 kg/m³. Considering the specified operating conditions for the multiphase pump outlined in this paper, the density of natural gas at the seabed is determined as 95.94 kg/m³ employing the ideal-gas equation, $PV = nRT$. The gas phase is assumed to consist of bubbles with a diameter of 0.1 mm, and the coalescence and fragmentation of bubbles between each other are not taken into account.

In the process of natural gas hydrate extraction, it is noteworthy that hydrate mineral particles may encompass varying proportions of seafloor sedimentary rock fragments. The density of the hydrate mineral particles can be calculated according to Equation (1) [22]:

$$\rho_s = (1 - S_T)\rho_\rho + S_T\rho_H \quad (1)$$

where ρ_s denotes the density of natural gas hydrate mineral particles; ρ_ρ represents the density of seafloor sedimentary debris; ρ_H signifies the density of natural gas hydrates; and S_T denotes the saturation of natural gas hydrates. Specifically, the density of natural gas hydrates is 920 kg/m³, while the density of seafloor sedimentary debris is approximately in the range of 1600 to 2200 kg/m³, with this study adopting a value of 2000 kg/m³. Employing a saturation range of 30% to 70% for natural gas hydrates, the density of hydrate particles is approximately between 1242 and 1676 kg/m³. However, for the purposes of simulation calculations in this research, a value of 1400 kg/m³ is employed for the density of hydrate particles. The solid-phase particle diameter in this study was set at 0.8 mm based on the study of natural gas hydrates by Huang Ting et al. [23].

In the actual operation of the pump, localized low pressure or even negative pressure can form near the inlet of the impeller and the suction side of the blades. The critical pressure for the phase transition of natural gas hydrates ranges between 18.4 and 130 MPa (specific values depend on the type of reservoir and the depth of the mineral layer) [24,25]. Under the agitation of the impeller, a certain amount of gas is inevitably generated. It is noteworthy, however, that the abundance of the gas phase does not exert any discernible impact on the rheological properties of the liquid phase. The central focus of this study revolves around the comparative analysis of the multiphase pump's performance under the influence of two distinct fluid types: non-Newtonian and viscous Newtonian fluids. In this study, the composition of each phase is as follows: the concentration of hydrate mineral particles is set at 25%, the gas phase occupies 5%, and the remaining constitutes the liquid phase (all in volumetric concentrations). To encapsulate these parameters, the medium conditions governing the operation of the multiphase pump designed for the extraction of marine natural gas hydrates in this study are presented in Table 1.

Table 1. Medium parameters for the operating conditions of the multiphase pump.

Medium	Density (kg/m ³)	Dynamic Viscosity (Pa·s)	Particle Sizes (mm)
Natural gas	95.94	7.207×10^{-6}	0.1
Hydrate particles	1400	0.00163	0.8
Sea water	1025	0.0017	/

Following the application of solid-state fluidization for marine natural gas hydrate extraction, a considerable quantity of seabed sediment clay becomes prevalent. Liu et al. [26] prepared hydrate muds with varying mass fractions using marine sediments from the

South China Sea as the substrate. Their primary focus was the in-depth exploration of the rheological characteristics exhibited by hydrate slurries across diverse seabed soil mass fraction conditions. Researchers such as SI [27] and Guo [28], among others, have similarly delved into examining the rheological properties of both seabed mud flow and hydrate-mixed slurries. The outcomes of these investigations reveal a notable non-linear relationship between the logarithmic coordinates of shear rate (γ) and apparent viscosity (μ_e) of the slurry. This intricate relationship is effectively captured by the Herschel–Bulkley rheological model, as illustrated by Equation (2) [29]. Wang [30] conducted experiments on non-Newtonian fluids, employing varied ratios of carboxymethyl cellulose (CMC) and bentonite. Through these experiments, Wang provided fitting parameters for the Herschel–Bulkley rheological model under normal temperature and pressure conditions. This model aptly approximates the complex rheological behavior observed in mud–water mixtures in close proximity to the seabed.

$$\mu_e = \frac{\tau_0}{\gamma} + K_a \cdot \gamma^{n-1} \quad (2)$$

where τ_0 represents the yield stress of the hydrate slurries (Pa); K_a is the consistency coefficient ($\text{Pa}\cdot\text{s}^n$); and n is the flow behavior index. As the shear rate exceeds a certain range, the alteration in the apparent viscosity of the fluid becomes trivial. Here, the shear rate range is set at 0.001 s^{-1} to 5000 s^{-1} . Detailed information concerning the rheological and physical attributes of the non-Newtonian working fluids utilized in this investigation is presented in Table 2. In this study, the fluid system involving seawater as its liquid phase is regarded as a viscous Newtonian fluid. Conversely, a fluid medium constituted by seabed hydrate minerals and clay is identified and categorized as a non-Newtonian fluid.

Table 2. Rheological and physical properties of operating solution.

Operating Solution	Density (kg/m^3)	Yield Stress (Pa)	Consistency ($\text{Pa}\cdot\text{s}^n$)	Flow Index
0.1%CMC and 8%Bentonite	1312	7.5	1.37	0.387

3. Numerical Methods

3.1. Governing Equations and Boundary Conditions

In this study, the Euler–Euler non-homogeneous phase model in ANSYS CFX is used to solve the “gas-liquid-solid” three-phase flow [31,32], and the following assumptions are made before numerical simulation:

- (1) Discrete and continuous phases are both regarded as continuous media, coexisting within the same spatial domain and sharing a common pressure field.
- (2) The “gas-liquid-solid” three-phase follows their respective mass and momentum control equations.
- (3) No mass transfer or chemical reactions occur between the phases, and there is no temperature variation during the flow process. Solid particles undergo no phase changes.

In this study, isothermal conditions are applied to the fluid domain, so the energy equation can be omitted. The mass conservation equation is as follows:

$$\frac{\partial}{\partial t}(\alpha_k \rho_k) + \nabla \cdot (\alpha_k \rho_k w_k) = 0 \quad (3)$$

Momentum equation

$$\frac{\partial}{\partial t}(\alpha_k \rho_k w_k) + \nabla \cdot (\alpha_k r_k w_k w_k - a_k \tau) = -\alpha_k \nabla p + \mathbf{M}_k + a_k r_k f_k \quad (4)$$

where subscript $k = l, g, \text{ or } s$ denotes the liquid, gas, or solid phase; ρ_k is the density; α_k is the volume fraction, and $\alpha_l + \alpha_g + \alpha_s = 1$; p is the pressure; and w_k, f_k , and M_k are the relative velocity, mass force, and interphase force per unit volume, respectively. τ denotes

the viscous stress tensor, which is related to the turbulent viscosity and molecular viscosity, and is expressed as Equation (5). Furthermore, based on the analysis by Yu et al. [33], in the operational phase of the pump, the Bassett and Magnus forces, the Saffman lifting force, and the turbulent dissipation force are not considered in order to simplify the calculations. Consequently, in the examination of inter-phase forces, this study solely contemplates the resistance induced by inter-phase velocity slip, pressure gradient forces, and virtual mass forces.

$$\tau_{ij} = 2\mu_k s_{ij} - \overline{\rho_k w'_{ki} w'_{kj}} \quad (5)$$

where $i, j = 1, 2, 3$ indicates the position of the three coordinate directions in the relative coordinate system; μ_k indicates the kinetic viscosity of each phase; S_{ij} denotes the strain tensor; and $-\overline{\rho_k w'_{ki} w'_{kj}}$ represents the turbulent Reynolds stresses caused by turbulent motion, and it can be derived by

$$-\overline{r_k w'_{ki} w'_{kj}} = 2\mu_{k,t} s_{ij} - \frac{2}{3}\rho_k d_{ij} \quad (6)$$

where $\mu_{k,t}$ indicates the turbulent viscosity. The shear-stress transport (SST) k - ω turbulence model exhibits robust adaptability in addressing flow separation phenomena induced by the shear-thinning characteristics in high-Reynolds-number flows [34]. Simultaneously, it demonstrates elevated precision in accurately solving near-wall flows in separated flow scenarios [35]. The turbulence viscosity calculation formula for this model is given as follows:

$$\mu_t = \frac{\rho a_1 k}{\max(a_1 \omega, SF_2)} \quad (7)$$

and

$$F_2 = \tanh\left(\arg_2^2\right) \quad (8)$$

$$\arg_2 = \max\left(\frac{2\sqrt{k}}{\beta'\omega y'}, \frac{500\nu}{y^2\omega}\right) \quad (9)$$

where S denotes the invariant measure of the strain rate; k is the turbulence kinetic energy; ω is the turbulence frequency; $a_1 = 5/9$; and $\beta' = 0.09$.

The inlet of the pump is governed by the inlet total pressure boundary condition, while the outlet is governed by the mass flow rate outlet boundary condition. A steady-state simulation was conducted by coupling the rotating domain (impeller) and stationary domain (inlet and outlet pipes and diffuser) using the Frozen Rotor model [36]. A rotor-stator transient model was used in the unsteady-state simulation. The interface between the diffuser and the outlet section was treated with the Frozen Rotor model for both steady and unsteady simulations. Unsteady calculations were initiated with the numerical results obtained from steady simulations as initial conditions to expedite convergence. The impeller shroud uses counter-rotating wall boundary conditions, while other walls are set as no-slip walls. A high-resolution scheme is applied for advection and turbulence terms.

3.2. Independence Test of Mesh and Time Step

A hexahedral structural mesh in Turbo-Grid and ICEM was used to mesh the multi-phase pump. The meshing diagram is presented in Figure 4, and the corresponding grid quality measurements are detailed in Table 3.

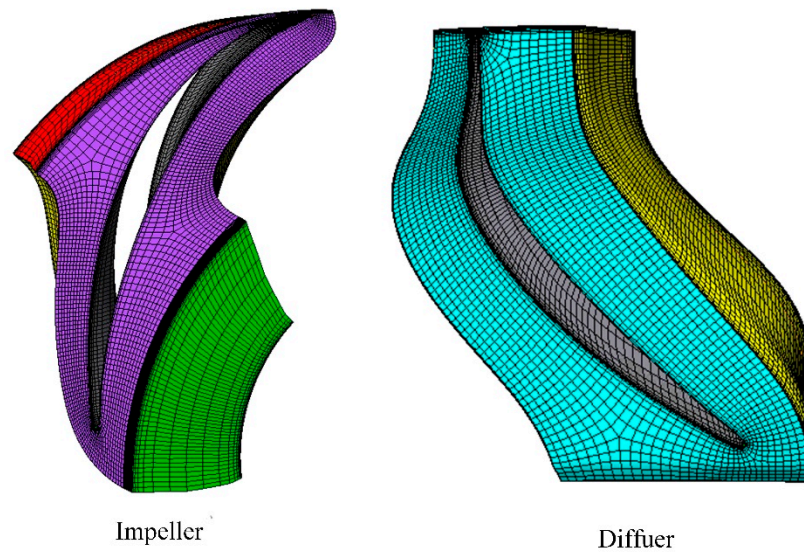


Figure 4. Schematic grid of impeller and diffuser.

Table 3. Grid quality measurement.

Mesh Measure	Value	%Bad
Minimum Face Angle	17.3103°	0.00
Maximum Face Angle	163.005°	0.00
Maximum Element Volume Ratio	14.2534	0.00
Minimum Volume	$2.634 \times 10^{-14} \text{ m}^3$	0.00
Maximum Edge Length Ratio	713.513	0.00
Maximum Connectivity Number	10	0.00

The grid independence of the single-stage booster device consisting of impeller, diffuser, and inlet and outlet pipe sections is verified using water as the flow medium. The ratio of the number of grids in each part of the single-stage booster unit and the independence test are shown in Figure 5. As depicted in Figure 5, the fluctuation rates of pressure increment and efficiency remain below 1.5% when the grid number exceeds G4, thereby aligning with the stipulated requirements for grid independence validation. In order to mitigate computational costs, subsequent numerical analyses are conducted utilizing the grid quantity corresponding to G4. Additionally, when the value of y^+ falls within the range of 10~66, it meets the calculation requirements for wall functions [37].

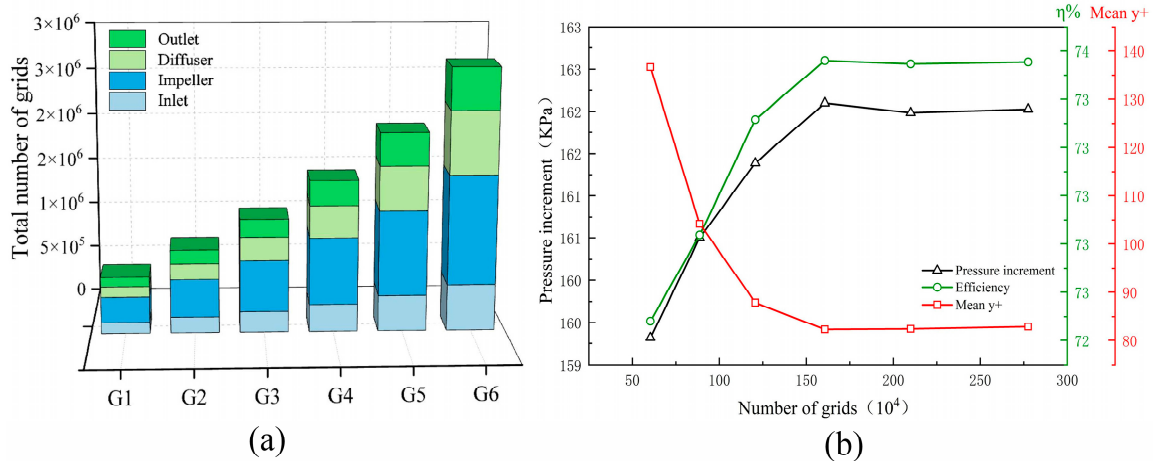


Figure 5. Schematic diagram of grid independence validation. (a) Number of meshes in different regions of the model; (b) grid independence verification.

Prior to undertaking a transient analysis of the multiphase pump, it is imperative to conduct a temporal independence analysis of the time steps employed in the transient analysis. In this paper, three time steps $\Delta t_1 = 7.14 \times 10^{-5}$ s, $\Delta t_2 = 9.52 \times 10^{-5}$ s, and $\Delta t_3 = 2.86 \times 10^{-4}$ s are chosen for the time-step independence testing. It is obvious from Figure 6 that the fluctuations of the pressure coefficient (C_p , defined as Equation (10)) at monitoring point P3 (marked in Figure 7) remain relatively consistent across the three temporal independence tests conducted at different time-step lengths. However, Δt_3 may cause data distortion due to fewer sampling points. Δt_1 and Δt_2 have enough sampling points with better data fluctuation coincidence, and Δt_2 is finally adopted by considering the computational cost and sampling accuracy.

$$C_p = \frac{p}{0.5\rho u^2} \quad (10)$$

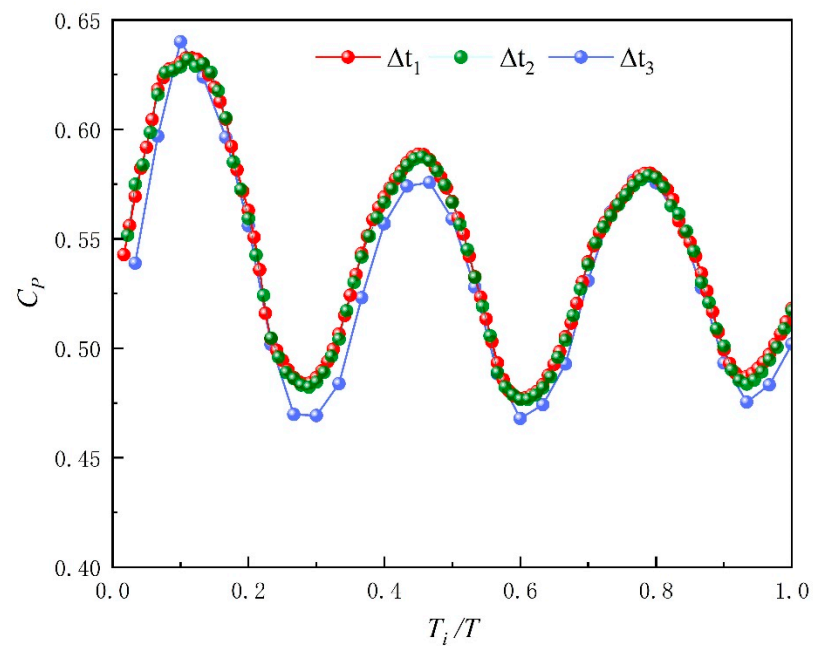


Figure 6. Independence test of time step.

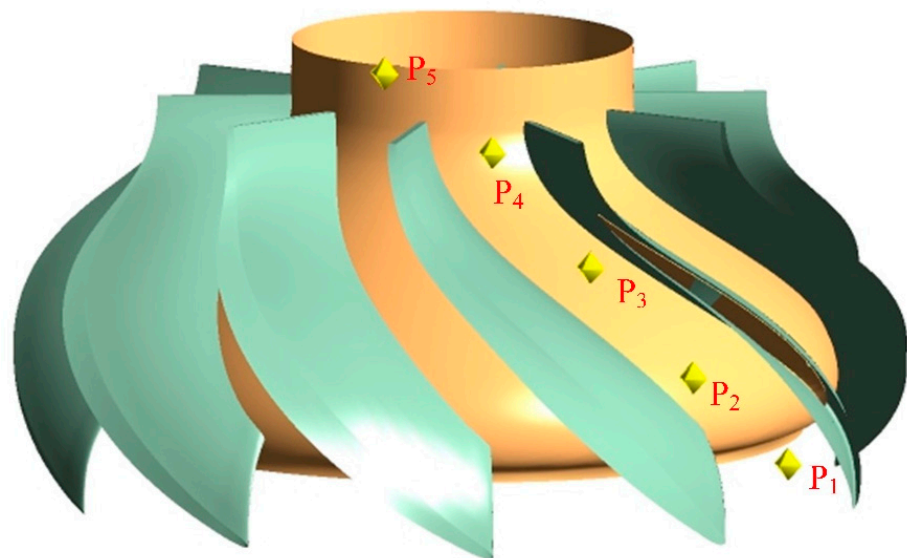


Figure 7. Schematic of the location of the monitoring points on the diffuser flow path.

In the unsteady-state simulation, five monitoring points were set up on the flow path from the diffuser inlet to the outlet, denoted as P_i ($i = 1\sim 5$). Among them, $P_1\sim P_4$ are located within the diffuser flow passage, and P_5 is positioned at the separation vortex on the trailing edge of the diffuser blades, as shown in Figure 7.

4. Results and Discussion

4.1. Validation of the Numerical Method

As illustrated in Figure 8, to validate the feasibility of the numerical approach described earlier, an experimental platform for the multiphase pump was constructed. This platform was designed to assess the performance disparities of the model pump in shear-thinning fluids and viscous Newtonian fluids. The acquisition of head data was executed by strategically situating pressure sensors at both the inlet and outlet of the experimental setup, thereby facilitating the measurement of pressure increments. The assessment of efficiency was predicated on the determination of the ratio between the effective power output and the motor's input power. Consequently, a multitude of parameters necessitated measurement, encompassing phase-specific flow rates, the motor's output torque, and rotational speed. Flow rates were measured using flow meters installed in the gas and liquid pipelines. Concurrently, torque and rotational speed were gauged via torque-speed sensors affixed to the motor coupler. The solid phase was prepared in a constant-volume mixing tank. Additionally, the adjustment of different flow rates is achieved through the coordinated operation of switch valves installed in the gas and liquid conduits, along with an electric control valve installed at the pump outlet. The primary instrumental and equipment parameters in the experimental setup are presented in Table 4. For non-Newtonian fluid testing, the chosen test medium involves a mixed solution prepared from carboxymethyl cellulose (CMC) and bentonite, as specified in Table 2. The density of the solution is confirmed using a density meter to ensure compliance with the required standards. The gaseous phase medium is supplied by a compressor, providing compressed air, while for the particulate phase, sand particles passing through a 20-mesh screen are utilized as a substitute for hydrate mineral particles.

Table 4. Parameters of the main components of the multiphase pump test system.

Apparatus	Production Type	Technical Specification	Measurement Accuracy
Motor	YVF2-225M-2	45 KW, 5~135 HZ	\
Torque sensor	ZH07	0~±200 N·m, 0~10,000 r/min	0.1~0.5 F·S
Electromagnetic flow meter	SZLDE-L	0~150 m ³ /h, 4~20 mA	\
Electric control valve	QB	4~20 mA	\
Pressure sensor	QDW90A	−0.1~0.1 MPa, 0~0.6 MPa	±0.03%FS/°C

Due to the intricacies of experimental conditions, variations in environmental parameters, and potential operational errors introduced by researchers, results obtained at different time points may exhibit disparities, thus incurring a certain degree of deviation. This discrepancy can be elucidated through uncertainty analysis. It is imperative to note that uncertainty analysis is not employed to ascertain the proximity of computed data to actual values. The performance analysis of the pump, encompassing parameters such as head and overall efficiency, adheres to the ISO 9906:2012 standard. This standard permits an uncertainty of 2% in the measurement of flow rate and uncertainties of 1.5% in the determination of head and efficiency. The present experiment was conducted under the operating conditions specified in the design point. The methods employed for the calculation of flow rate, head, and efficiency bear resemblance to those reported by Sun et al. [38]. The uncertainty of the measured results was evaluated at 1.1% of the pump head, 2.4% of the pump efficiency, 0.15% of the motor speed, and 0.2% for inlet gas volume fraction (IGVF). These evaluations are grounded in the observed fluctuations during the experimental testing process.

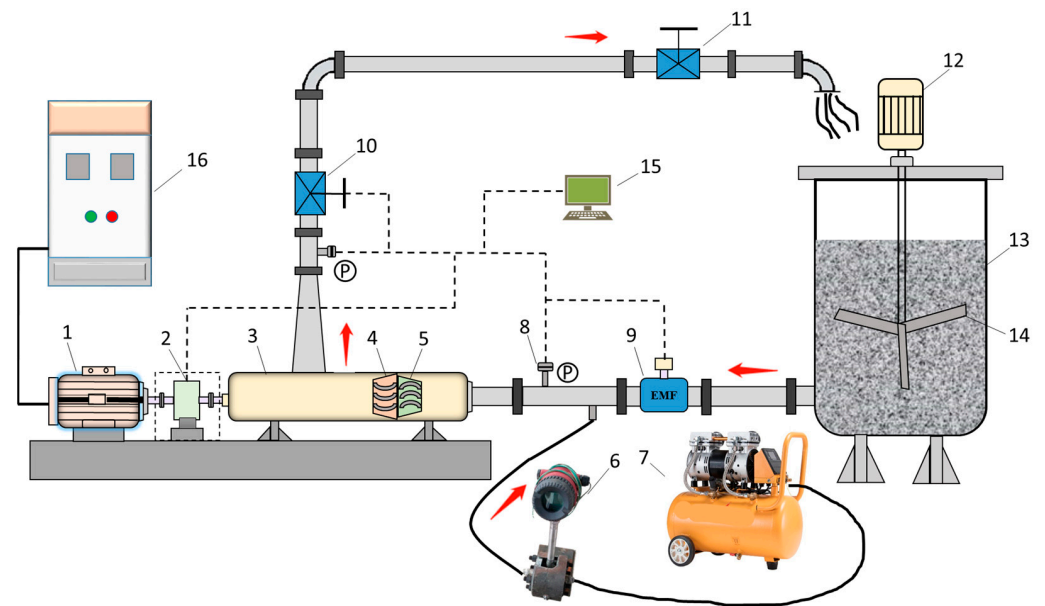


Figure 8. Schematic diagram of the experimental process of multiphase pump. (1) High-speed variable-frequency motor; (2) torque sensor; (3) multiphase pump tooling bench; (4) diffuser; (5) impeller; (6) gas flow meter; (7) air compressor; (8) pressure sensor; (9) electromagnetic flow meter; (10) electric control valve; (11) gate valve; (12) mixing motor; (13) liquid-solid mixing tank; (14) mixing blades; (15) data collection center; (16) frequency inverter cabinet.

Figure 9 presents the efficiency and pressure-increment curves for this multiphase pump for transporting non-Newtonian fluids with shear-thinning characteristics and viscous Newtonian fluids. Due to the absence of considerations for volumetric losses and mechanical friction losses in the simulation calculations, the simulated performance curves are higher than the experimental results. Under design conditions, the efficiency and pressure-rise errors between non-Newtonian fluid simulation and experimentation are 8.07% and 7.52%, respectively. Furthermore, the mean absolute percentage errors (MAPE) for efficiency and pressure increment are 8.93% and 7.91%, respectively. Therefore, it can be concluded that the numerical methods used in this study are reliable.

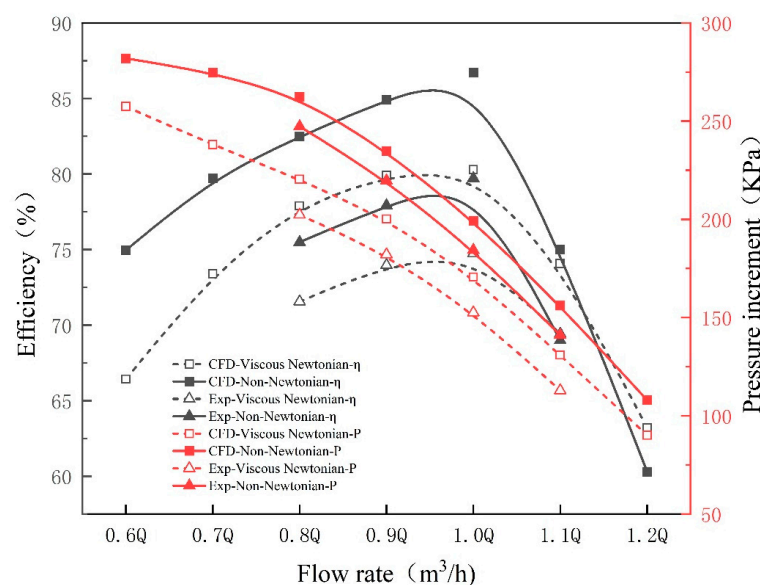


Figure 9. Efficiency and pressure-increment curves with two fluids.

4.2. Variation of Apparent Viscosity

In the transient simulations in this paper, using the steady-state results as the initial conditions, a one-half revolution of the impeller was considered as one complete cycle, and a total of 12 cycles were simulated, resulting in a total of 1080 sampling points. In the following analysis, the dimensionless intensity ($C_{I\mu a}$) of the apparent viscosity variation is defined as [39]

$$C_{I\mu a} = \frac{I_{\mu a}}{0.5\rho u d} \quad (11)$$

$$I_{\mu a} = \sqrt{\frac{1}{N} \sum_{i=1}^N (\mu_{a_i} - \bar{\mu}_a)^2} \quad (12)$$

$$\bar{\mu}_a = \frac{1}{N} \sum_{i=1}^N \mu_{a_i} \quad (13)$$

where N represents the number of sampling points; $I_{\mu a}$ stands for the intensity of apparent viscosity variation; $\bar{\mu}_a$ represents the average apparent viscosity; $\mu_{a,i}$ represents the apparent viscosity at each time step; u is the circumferential velocity at the impeller outlet; and d is the impeller outlet diameter.

Figure 10 illustrates the distribution of $C_{I\mu a}$ at different blade heights (Span = 0.1, 0.5, 0.9) for all sampling points at the design flow rate. As per Equation (2), the variation of apparent viscosity is inversely proportional to the shear rate. Therefore, Figure 11 depicts the distribution of shear rate γ at the same positions as Figure 11. It can be observed that after the fluid enters the impeller region, the $C_{I\mu a}$ values significantly decrease. Upon passing through the diffuser into the outlet pipe section, the $C_{I\mu a}$ values begin to increase significantly due to the decrease in flow velocity. At Span = 0.1 and Span = 0.9, the apparent viscosity $C_{I\mu a}$ values are noticeably lower than the level at Span = 0.5. This is attributed to the increased frictional shear stress near the wall surfaces (Hub, Shroud), leading to higher shear rates (corresponding to Figure 11) and, consequently, higher $C_{I\mu a}$ values at Span = 0.5 compared to the regions near the hub and shroud.

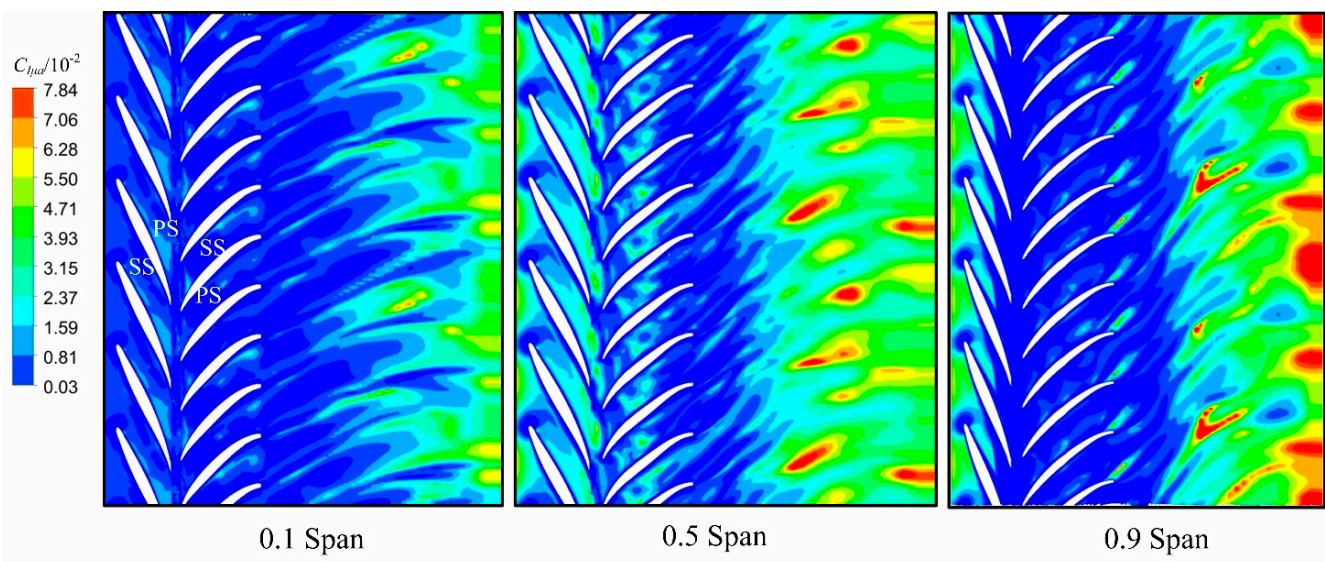


Figure 10. Intensity of apparent viscosity variation on turbo-surfaces.

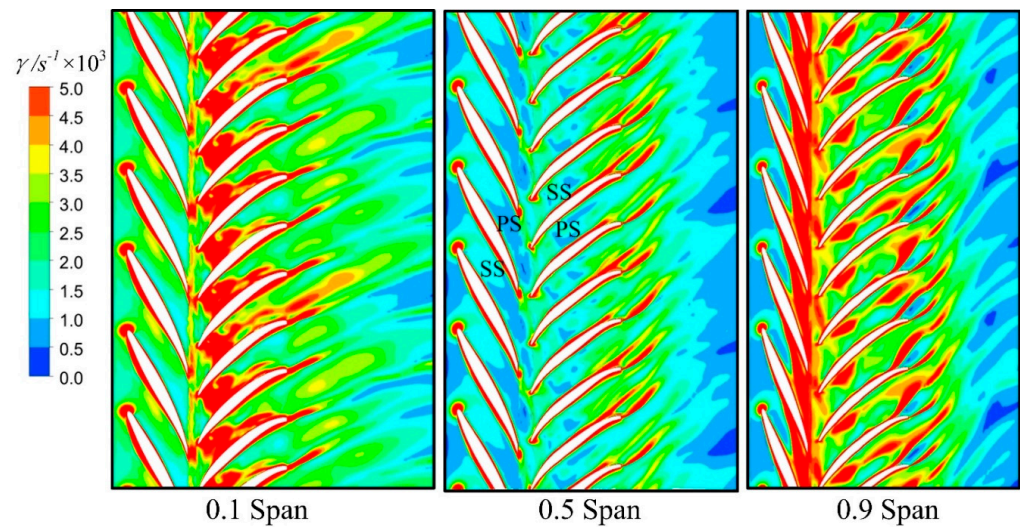


Figure 11. Variation of shear strain rate in a multiphase pump flow channel.

In Figure 11, it is evident that at Span = 0.1 and Span = 0.9, the shear rate in both the impeller and diffuser regions is comparatively higher when juxtaposed with the shear rate in the impeller region alone. This discrepancy arises due to the elevated wall shear stress present in the proximity of the near-wall region, particularly noted at Span = 0.1 and Span = 0.9 spans. Under the effect of wall shear thinning, the wall friction decreases, resulting in a reduction in wall shear stress, an increase in fluid velocity, and a corresponding increase in shear rate. Simultaneously, the shear rate in the diffuser region is relatively higher compared to the impeller region. This is due to the increase in kinetic energy within the impeller region, which is converted into pressure energy upon entering the diffuser channel, resulting in an increase in flow instability. This phenomenon is also evident in Figure 12, where the shear rate values within the diffuser are slightly higher than those within the impeller region.

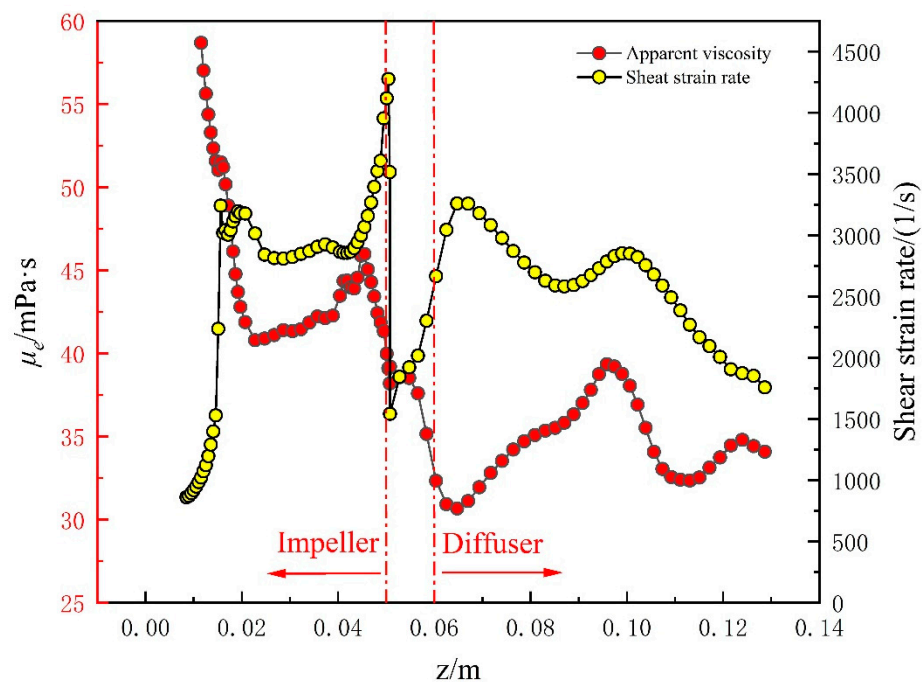


Figure 12. Variation of apparent viscosity and shear rate along the flow direction in a multiphase pump flow channel.

In Figure 12, it is evident that upon the fluid's ingress into the impeller channel, the impeller's rotational motion induces a marked escalation in fluid velocity, resulting in a noteworthy upsurge in shear rate. Under the influence of shear thinning, the apparent viscosity decreases significantly. In the region proximate to the blade trailing edge and in the absence of blades, the shear rate undergoes an initial ascent due to the dynamic–stationary interaction between the impeller and the diffuser. Subsequently, there is an abrupt descent, succeeded by a gradual reascension. This corresponds to a decrease in apparent viscosity, followed by a slight increase before decreasing again. As the fluid progresses into the diffuser passage, the conversion of kinetic energy to pressure energy leads to heightened flow instability, causing the shear rate to first increase and then decrease. Owing to the influence of the separation vortex at the trailing edge of the diffuser blades, the shear rate of the fluid exhibits fluctuations subsequent to its passage over the trailing edge of the diffuser blades. Analogously, the alterations in apparent viscosity within the flow trace an opposing trajectory, all of which can be elucidated by the impact of fluid shear thinning.

4.3. Discussion of the Evolution of Vortex Structures

In order to investigate the influence of shear-thinning characteristics on the evolution and development of vortex structures within the flow field when multiphase pumps are employed for transporting non-Newtonian and viscous Newtonian fluids, this study conducted a comparative analysis of these two fluid types. Both of these fluids exhibit comparable density and surface tension properties. Figure 13 presents the vortex structure at the trailing edge of the diffuser at Span = 0.5 under the influence of non-Newtonian and viscous Newtonian fluids. An interesting observation is that in Figure 14a, under the influence of the non-Newtonian fluid, there are two vortices (Vortex A, Vortex B) at the trailing edge of blade D1. In Figure 14b, under the influence of the viscous Newtonian fluid, blade D1's trailing edge vortex consists of only one vortex (Vortex C).

To better explain the phenomenon described above, Figure 14 provides pressure distribution and velocity vector contours of the flow field under the influence of two different fluids. It is well known that vortices are formed due to the difference in pressure gradient between the pressure side (PS) and the suction side (SS) of the pump blades, causing low-speed fluid to shift toward the SS. Additionally, the pressure gradient at the SS in the downstream direction leads to flow separation, resulting in the formation of Vortex A. The formation of Vortex B is the result of the interaction between the main flow and the reverse flow pressure gradients. Furthermore, due to the lower friction losses when dealing with a non-Newtonian fluid, the velocity gradient between PS and SS is larger under the influence of the non-Newtonian fluid compared to the case with a viscous Newtonian fluid. Consequently, the vortex scales are larger under the influence of the non-Newtonian fluid compared to the viscous Newtonian fluid. Moreover, in Figure 13a, the shear-thinning characteristics of the fluid are evident, leading to a significant interaction between the trailing-edge vortex and the main flow, as depicted in Figure 10. This interaction region exhibits a pronounced apparent viscosity variation.

In a viscous Newtonian fluid, as shown in Figure 13b, the generation and evolution pattern of trailing edge vortices are generally similar to those in a non-Newtonian fluid, but the scales are noticeably smaller. One reason is the shear-thinning property, which reduces the flow resistance. On the other hand, non-Newtonian fluids have higher flow velocities, and the kinetic energy is relatively higher compared to viscous Newtonian fluids. In Figure 7, five monitoring points (P1–P5) are uniformly placed along the flow direction inside the diffuser to quantitatively characterize the evolution of the vortex structure. P4 is located at the exit of the diffuser channel, while P5 is located at the separation vortex of the diffuser blade's trailing edge.

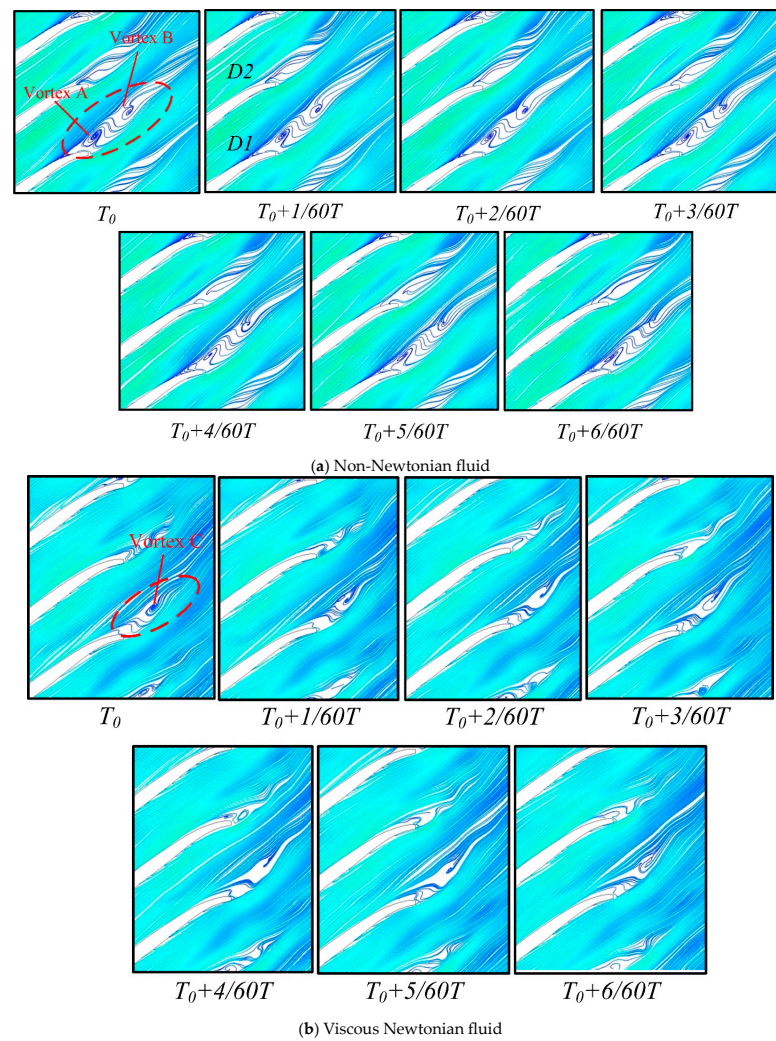


Figure 13. Evolution of vortex structure on the turbo-surface of 0.5 span (*D1* and *D2* are the blade numbers of the diffuser).

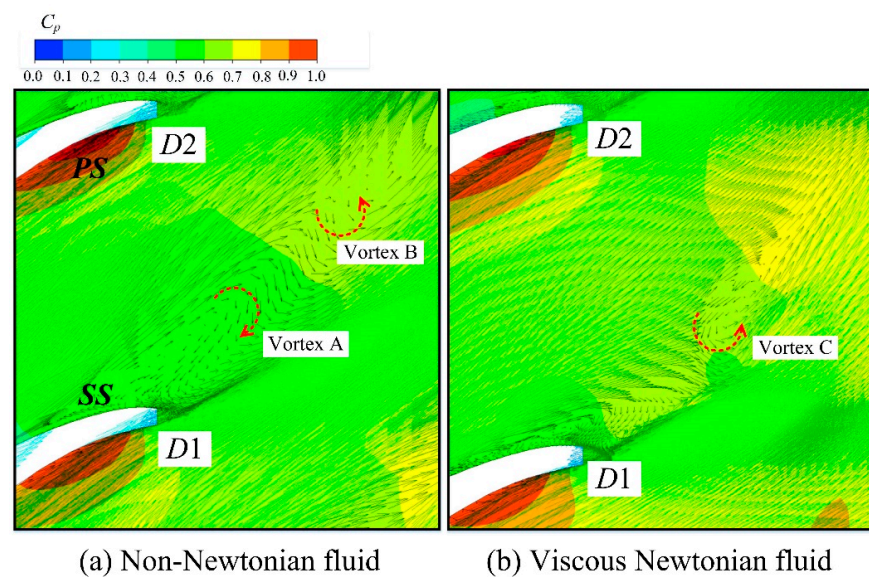


Figure 14. Distributions of the pressure and the velocity vectors.

Figure 15 presents the variation of vorticity over time at monitoring points P4 and P5 during a rotor revolution. At point P4, both fluids exhibit three peaks and valleys, corresponding to half of the blade number, which confirms the strong influence of dynamic and static interaction on vortex evolution. In each cycle, the change in the vorticity strength of the non-Newtonian fluid is greater and more unstable and has higher amplitude compared to the viscous Newtonian fluid. At point P5, due to the influence of trailing edge separation vortices, the non-Newtonian fluid displays regular fluctuations between peaks and valleys, forming a small oscillation cycle. Simultaneously, in the waveform of the viscous Newtonian fluid, anomalous curves are observed due to the influence of trailing edge separation vortices as well. Overall, the strength of vortex evolution is stronger for the non-Newtonian fluid relative to the viscous Newtonian fluid at points P4 and P5, which further suggests that the shear-thinning characteristics promote the instability of the flow.

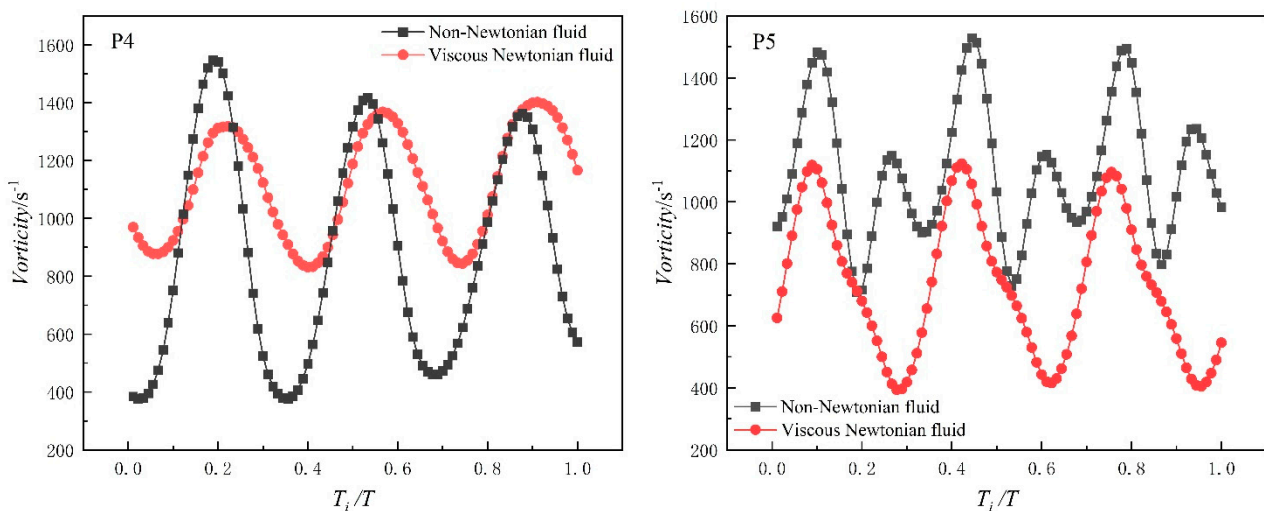


Figure 15. Variation of vorticity with time at monitoring points P4 and P5.

4.4. Discussion of Pressure Fluctuation Characteristics

Based on the simulation results, the pressure fluctuation characteristics at the monitoring points shown in Figure 16 were analyzed using the fast Fourier transform (FFT) method. The design rotational speed of the multiphase pump is 3500 r/min, which yields a rotational frequency of $f_i = 3500/60 = 58.33$ Hz.

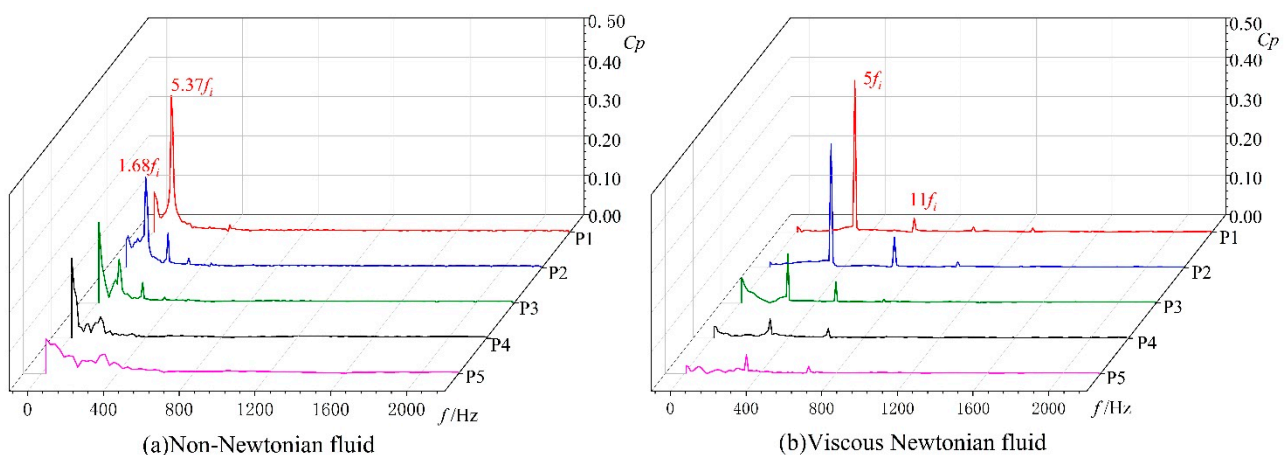


Figure 16. Frequency spectra of pressure fluctuations.

In viscous Newtonian fluids, the primary frequency at each monitoring point predominantly occurs at around 307 Hz, while the secondary frequency is mainly observed

near 615 Hz. This means that the primary and secondary frequencies are approximately $5f_i$ and $11f_i$, respectively. This indicates that in viscous Newtonian fluids, the dominant factor influencing pressure fluctuations is the interaction between the rotor and stator.

Compared to viscous Newtonian fluids, the pressure fluctuation characteristics of non-Newtonian fluids are more complex. In the non-Newtonian fluid, the primary frequencies at P1 and P2 are mainly around 23 Hz, while the primary frequencies at P3–P5 are primarily around 20 Hz. Except for P1, the secondary frequencies at all other points are mainly around 210 Hz. P1 and P2 near the diffuser inlet are significantly influenced by the dynamic and static interaction between the rotor and stator. The influence of rotor–stator interaction on flow instability diminishes gradually along the flow direction, while the impact of shear-thinning characteristics proportionally intensifies. As delineated in Table 5, the amplitude of the secondary frequency surpasses that of the primary frequency, signifying the predominant role of shear-thinning characteristics in inducing flow instability within the downstream channel. Furthermore, the non-Newtonian fluid exhibits an increased prevalence of low-frequency components in pressure fluctuations. From the aforementioned observations, it becomes evident that in the viscous Newtonian fluid, the interaction between the rotor and stator predominantly governs pressure fluctuations. In contrast, within the realm of non-Newtonian fluid dynamics, pressure fluctuations are subject to the interplay between the rigidity of the rotor–stator interaction and the influence of shear-thinning characteristics.

Table 5. Amplitude of pressure coefficient fluctuations at each monitoring point.

	Dominant Frequency		Secondary Frequency	
	Non-Newtonian Fluid	Viscous Newtonian Fluid	Non-Newtonian Fluid	Viscous Newtonian Fluid
P1	$1.68f_i$	$5.37f_i$	$0.13f_i$	$10.75f_i$
P2	$1.88f_i$	$5.74f_i$	$3.9f_i$	$11.48f_i$
P3	$0.15f_i$	$4.35f_i$	$1.98f_i$	$8.69f_i$
P4	$0.22f_i$	$5.27f_i$	$2.83f_i$	$10.53f_i$
P5	$0.82f_i$	$5.63f_i$	$5.74f_i$	$11.27f_i$

To evaluate the pressure fluctuation characteristics within a multiphase pump flow channel, the dimensionless intensity of pressure fluctuations is used [39]:

$$C_{IPF} = \frac{I_{PF}}{0.5\rho u_2^2} \quad (14)$$

$$I_{PF} = \sqrt{\frac{1}{N} \sum_{i=1}^N (p_i - \bar{p})^2} \quad (15)$$

$$\bar{p} = \frac{1}{N} \sum_{i=1}^N p_i \quad (16)$$

where I_{PF} represents the intensity of pressure fluctuations, and p_i and \bar{p} are the instantaneous pressures and average pressures, respectively.

From Figure 17, four high C_{IPF} regions can be observed, namely Regions A, B, C, and D. Among them, Region A is located at the inlet of the diffuser, and the flow state in this region is mainly influenced by the dynamic and static interaction between the rotor and stator. The flow state differs slightly between non-Newtonian and viscous Newtonian fluid conditions. In non-Newtonian fluids, the C_{IPF} intensity at the leading edge of the diffuser blades is significantly higher than in viscous Newtonian fluids, corresponding to more intense pressure fluctuations at point P1 in Figure 16. Regions B and C are located near the leading and trailing edges of the diffuser blades on the PS side. Due to the strong shear-thinning characteristics of non-Newtonian fluids, the fluid velocity

is higher, and fluid kinetic energy is greater in these regions. As a result, the pressure energy converted here is greater compared to viscous Newtonian fluids, corresponding to monitoring points P2 and P4 in Figure 16. Additionally, in the middle of the blades between Regions B and C, the pressure is relatively low, corresponding to lower pressure fluctuation amplitudes at monitoring point P3 in Figure 16. Region D is located near the separation vortex at the trailing edge of the diffuser blades, as depicted in the streamline distribution in Figure 13. This region represents the interaction zone between the main flow and the trailing edge separation vortex. In the case of non-Newtonian fluids, as described in Section 4.3, under the interaction of the main flow and trailing edge separation vortex, pressure fluctuations in this region are stronger compared to viscous Newtonian fluids. Therefore, when transporting non-Newtonian fluids, pressure fluctuations are enhanced, especially in Regions C and D, due to the shear-thinning characteristics.

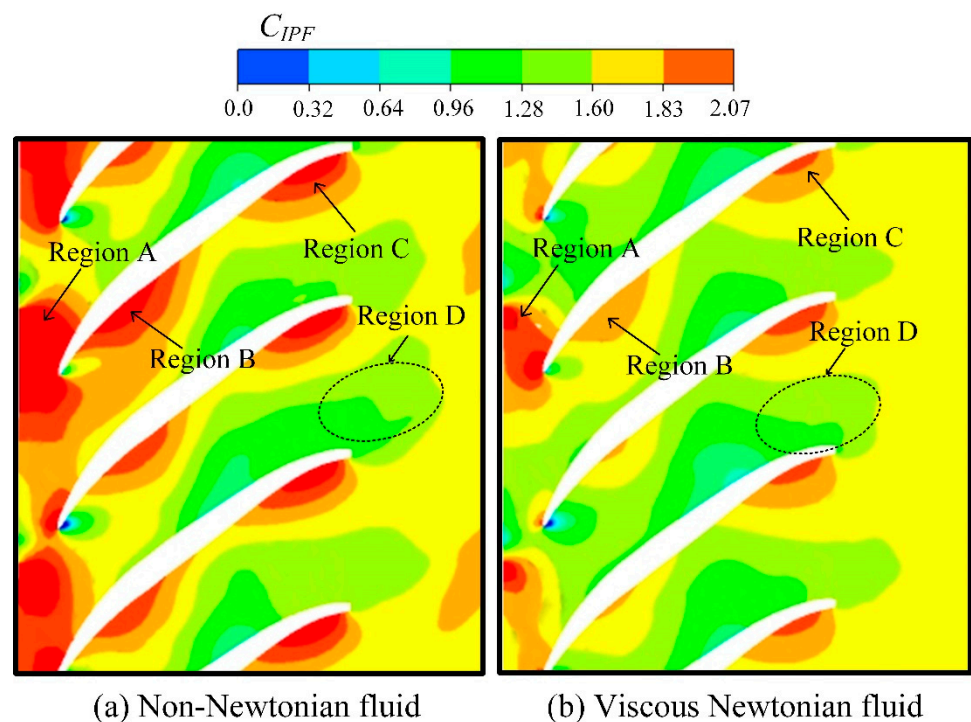


Figure 17. Distribution of CIPF on the turbo-surface of 0.5 span.

4.5. Influence of Gas-Solid Two-Phase Distribution

Figures 18 and 19 illustrate the temporal evolution of the gas volume fraction on the pressure side of the impeller in both non-Newtonian and viscous Newtonian fluids. As discernible from the illustration, in non-Newtonian fluids, the uniform distribution of the gas phase occurs on the PS of the blades, whereas in viscous Newtonian fluids, the gas phase predominantly occupies the vicinity of the trailing edge on the PS of the blades. This phenomenon is attributed to the distinctions in shear forces and shear rates between the two fluid types. In the region adjacent to the trailing edge of the blade, where the pressure is relatively high and the flow velocity is rapid, substantial shear forces result in a higher volume fraction of the gas phase being transported to this area. In contrast, the rheological properties undergo a transformation in non-Newtonian fluids, wherein the apparent viscosity demonstrates a more pronounced variation with shear rate. The enhanced shear deformation capability of non-Newtonian fluids on the pressure side of the blade facilitates the gradual filling of the entire pressure surface with gas-phase distribution, particularly under conditions of high shear rates.

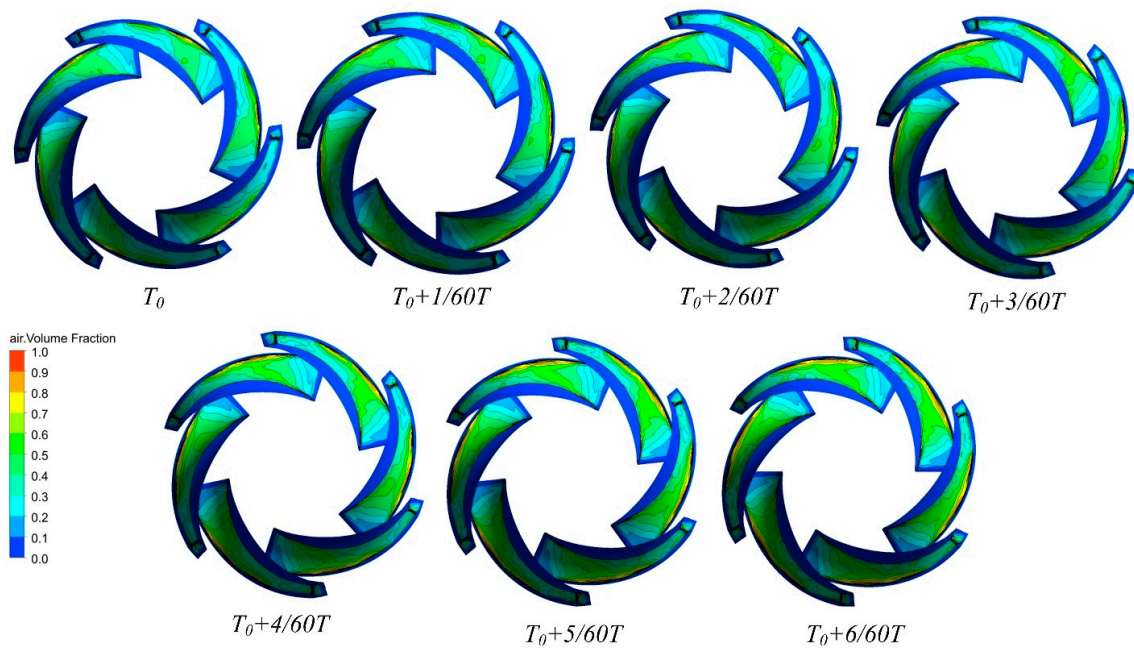


Figure 18. Distribution of gas volume fraction at the impeller's PS in non-Newtonian fluid.

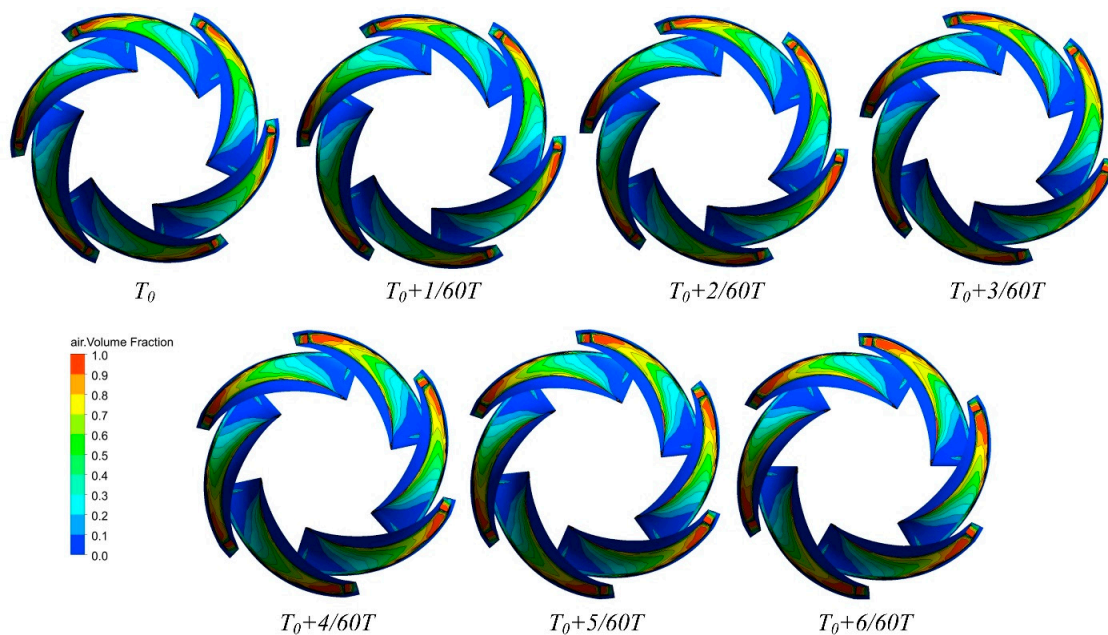


Figure 19. Distribution of gas volume fraction at the impeller's PS in Newtonian fluid.

Figures 20 and 21 present the distribution of the gas volume fraction at a height of $\text{Span} = 0.5$ in non-Newtonian and viscous Newtonian fluids. From the figure, it can be seen that in the non-Newtonian fluid, the gas volume fraction is uniformly distributed in the impeller channel, and the distribution of the gas volume fraction is essentially the same on the PS and SS surfaces. In contrast, in the viscous Newtonian fluid, the distribution of gas volume fraction within the impeller passage is inhomogeneous, with the gas volume fraction on the SS side significantly higher than that on the PS side. Moreover, with the passage of time, the fluid with a higher gas fraction at the SS trailing edge flows through the PS of the subsequent blade, leading to an increase in the gas volume fraction at the trailing edge of the PS blade. This phenomenon is also consistent with the distributions shown in Figures 18 and 19.

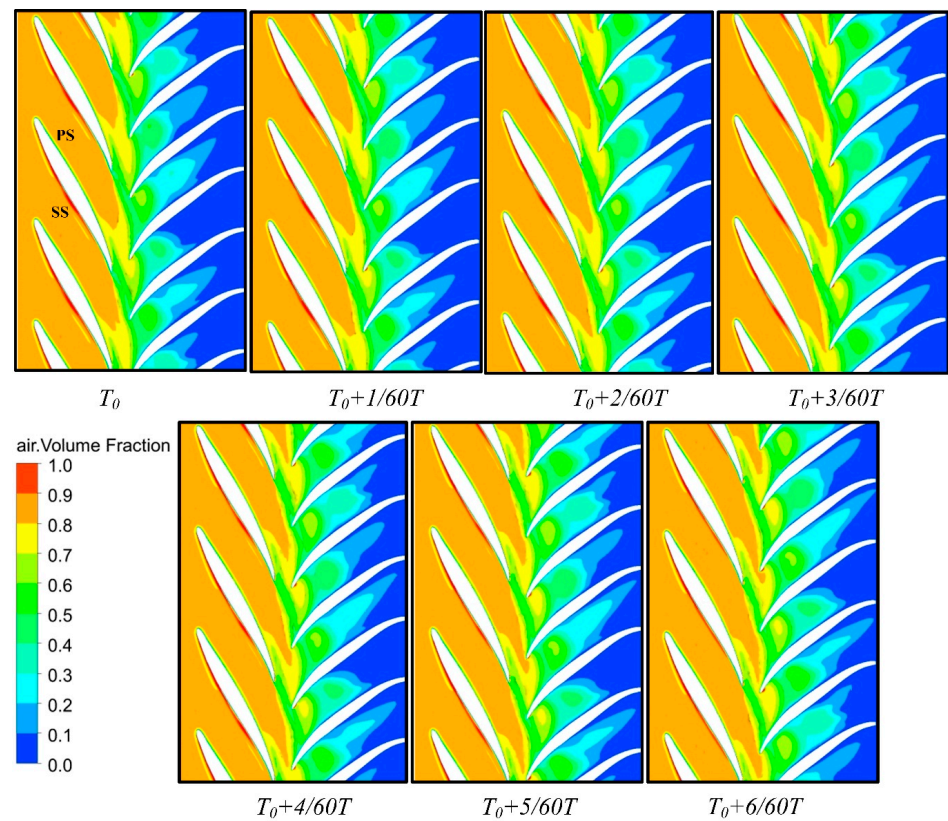


Figure 20. The degree of change in the gas-phase volume fraction on the turbo-surface in non-Newtonian fluid.

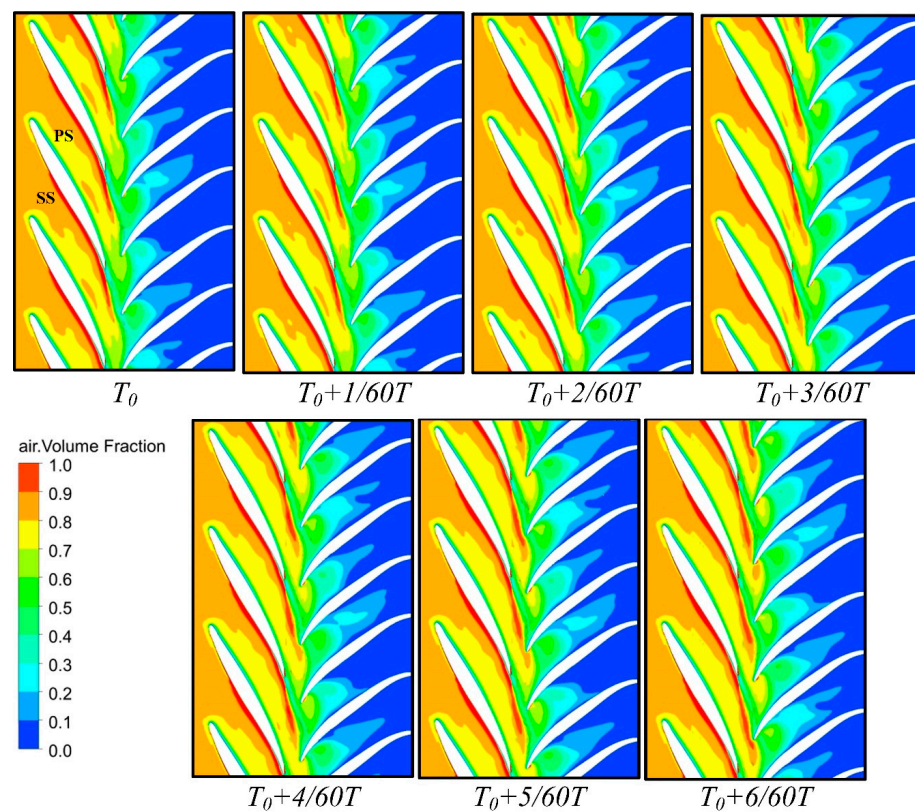


Figure 21. The degree of change in the gas-phase volume fraction on the turbo-surface in Newtonian fluid.

Figures 22 and 23 illustrate the temporal evolution of the solid volume fraction distribution on the PS of the impeller in both non-Newtonian and viscous Newtonian fluids. In the viscous Newtonian fluid, the concentration of the solid volume fraction at the leading edge of the impeller's PS is primarily attributed to the action of shear forces and shear rates. When the fluid traverses the leading edge of the blade, the interplay of geometric shape and rotational motion generates regions characterized by high-speed flow and significant shear forces. These forces efficiently propel solid particles away from the PS of the blade post-leading edge passage, consequently leading to an accumulation of solid volume fraction in the vicinity of the leading edge region under the specified conditions. However, in the non-Newtonian fluid, the apparent viscosity exhibits a more pronounced variation with shear rate. Under the influence of shear thinning, solid particles become more mobile with the fluid flow, and in conjunction with the effect of fluid viscosity, the coverage area of solid particles on the impeller's PS increases.

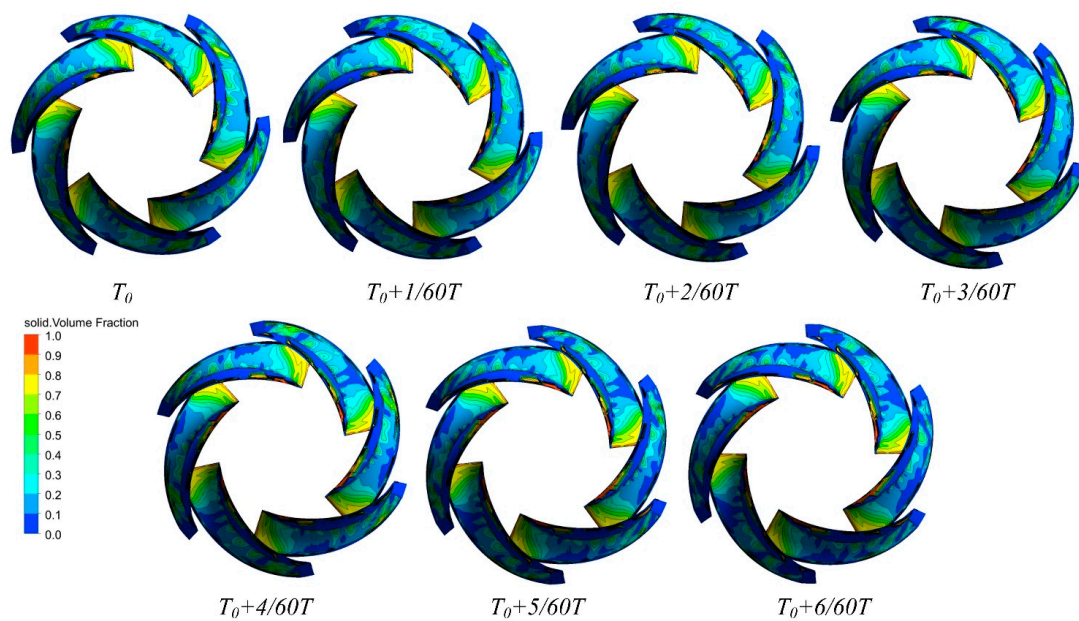


Figure 22. Distribution of solid volume fraction at the impeller's PS in non-Newtonian fluid.

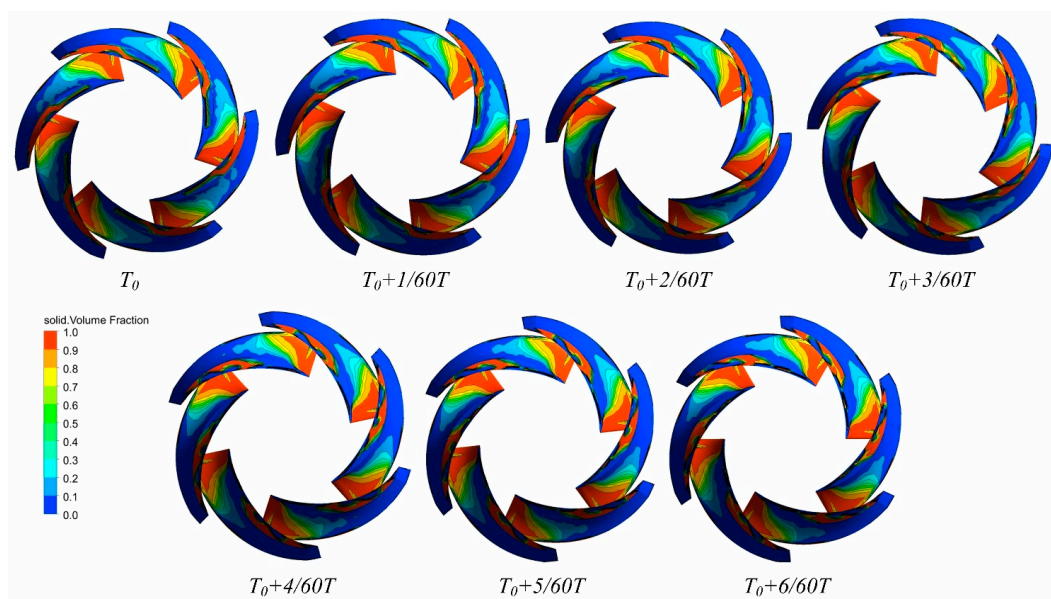


Figure 23. Distribution of solid volume fraction at the impeller's PS in Newtonian fluid.

Figures 24 and 25 present the distribution of the solid volume fraction at Span = 0.5 of the blade height in non-Newtonian and viscous Newtonian fluids. From the graphs, it can be observed that in the non-Newtonian fluid, the distribution of the solid volume fraction on the impeller's PS is more uniform compared to the viscous Newtonian fluid. This is primarily evident in the viscous Newtonian fluid where the solid volume fraction decreases near the trailing edge of the blade on the PS, whereas in the non-Newtonian fluid, the solid volume fraction is more consistently distributed across the PS. This observation aligns with the phenomena observed in Figures 22 and 23.

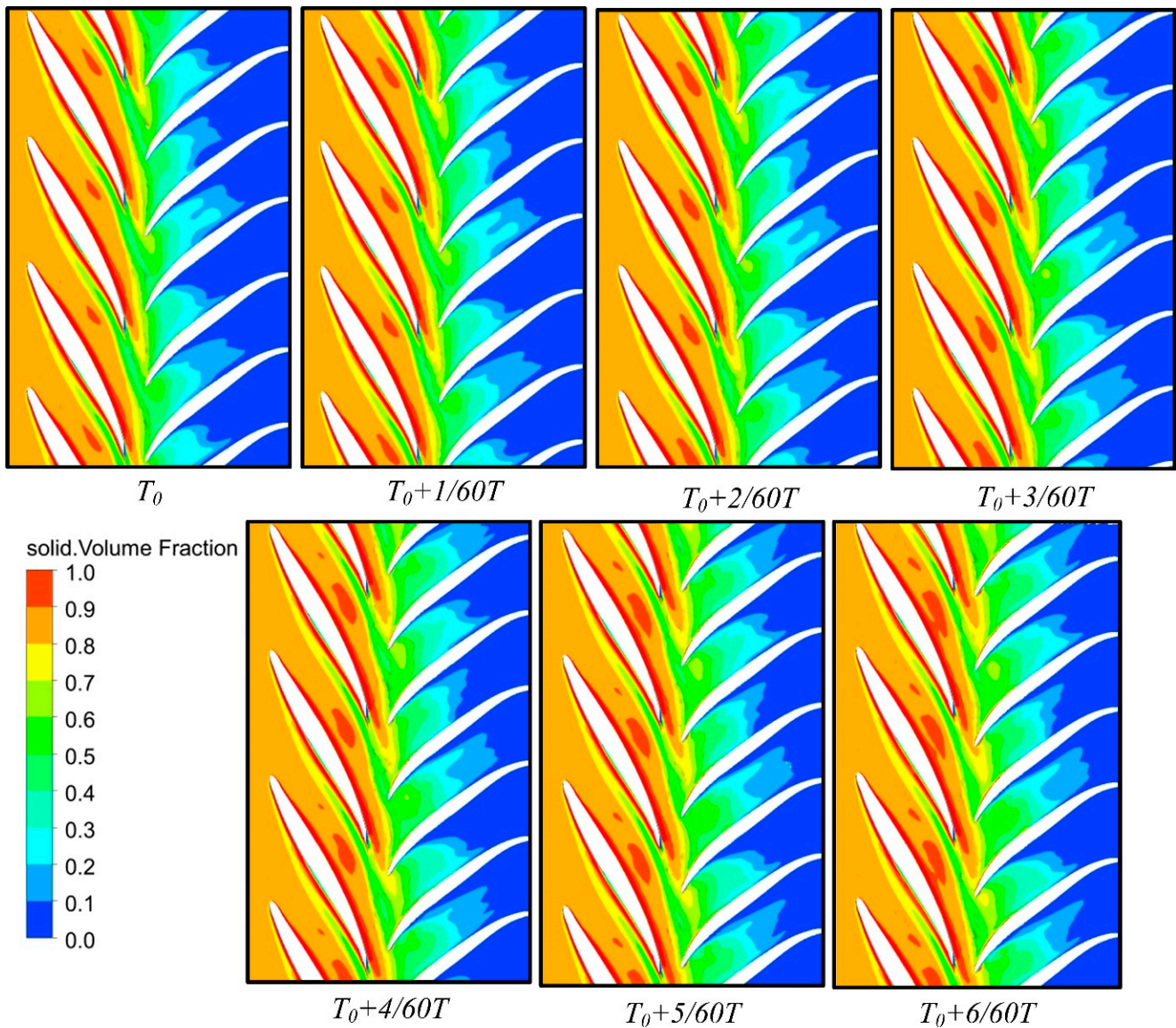


Figure 24. The degree of change in the solid volume fraction on the turbo-surface in non-Newtonian fluid.

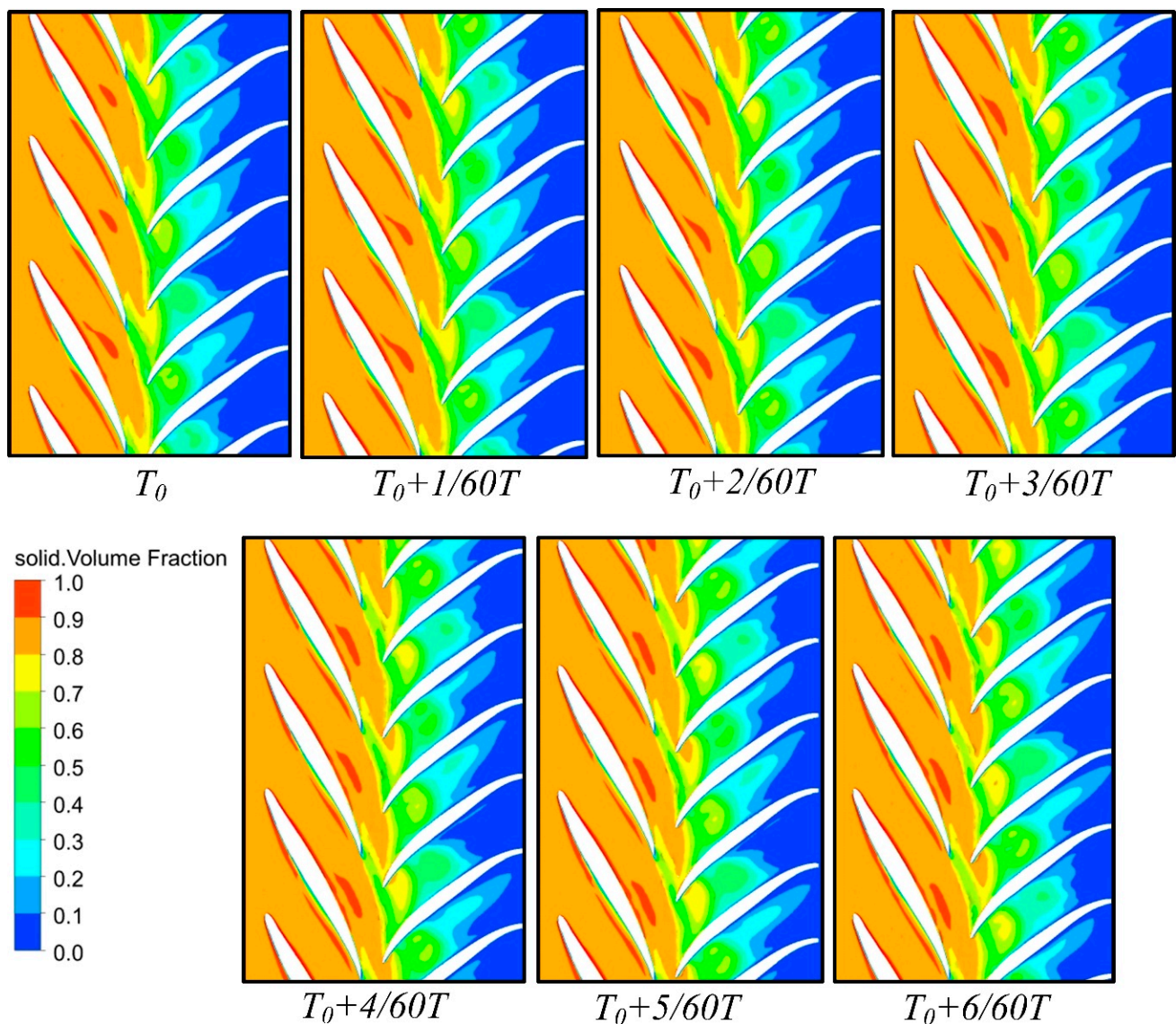


Figure 25. The degree of change in the solid volume fraction on the turbo-surface in Newtonian fluid.

5. Conclusions

This study, built upon experimental investigations and CFD simulations, delves into the evolution of vortex structures, pressure fluctuations, and the influence of shear-thinning characteristics on the distribution patterns of gas-solid two-phase flow in a multiphase pump operating within non-Newtonian and viscous Newtonian fluids. The primary conclusions derived from this research are summarized as follows:

1. The shear rate in the impeller is significantly higher than that in the diffuser, but the apparent viscosity changes considerably in the rear region of the diffuser. The presence of trailing-edge separation vortices significantly contributes to pronounced fluctuations in apparent viscosity at this location.
2. In the case of non-Newtonian fluids, flow separation near the SS, induced by pressure-gradient-related effects along the flow direction, gives rise to Vortex A. Furthermore, the interaction of pressure gradients in both the mainstream and backflow directions forms Vortex B. While the mechanism for vortex structure formation in a viscous Newtonian fluid is broadly similar to that in a non-Newtonian fluid, the shear-thinning characteristics of the latter result in faster flow velocities and lower friction losses. Consequently, the velocity gradient between the primary and secondary flows is

- greater in the non-Newtonian fluid, leading to larger-scale vortex structures under their influence.
3. Under the conditions of a viscous Newtonian fluid, pressure fluctuations primarily stem from the dynamic interaction between the rotor and stator. Conversely, when conveying a non-Newtonian fluid, the inducing factors for pressure fluctuations result from the combined effects of dynamic interaction and shear-thinning characteristics. Additionally, shear-thinning characteristics contribute to certain low-frequency components of pressure fluctuations.
 4. The high-magnitude regions of pressure fluctuations in both fluids are similar. However, due to shear-thinning characteristics, non-Newtonian fluids exhibit enhanced vortex fluctuations, leading to increased pressure fluctuation intensity, particularly at the locations of trailing-edge separation vortices.
 5. Moreover, the distribution behavior of gas-solid two-phase flow on the PS of the impeller differs slightly under the influence of the two fluids. In a non-Newtonian fluid, the distribution of gas-solid two-phase flow on the PS is more uniform compared to that in a viscous Newtonian fluid. In a viscous Newtonian fluid, the gas phase is distributed closer to the trailing edge of the blade of the PS, while the solid phase is distributed closer to the leading edge. The shear-thinning characteristics of the non-Newtonian fluid play a crucial role in this observed behavior.

This study delves into the characteristics of a multiphase pump employed during the extraction phase of natural gas hydrates, focusing on the evolution of vortex structures and pressure fluctuations under the influence of non-Newtonian and viscoelastic Newtonian fluids. However, in practical field applications, the flow patterns of incoming gas bubbles and the distribution of solid phases can contribute to flow instability and pronounced pressure fluctuations. In the subsequence of this research, a hybrid approach incorporating experimental and computational fluid dynamics will be employed to investigate the phenomenon of unsteady flow in different bubble flow patterns within non-Newtonian fluids.

Author Contributions: Conceptualization, L.C. and Y.Y.; methodology, L.C.; software, L.C.; validation, Y.Y.; formal analysis, Y.G.; investigation, L.C., C.P., X.Z. and Y.Y.; resources, Y.Y. and X.Z.; data curation, L.C. and Y.G.; writing—original draft preparation, L.C.; writing—review and editing, L.C. and Y.Y.; visualization, L.C. and Y.Y.; supervision, Y.Y. and X.Z.; project administration, Y.Y. and X.Z.; funding acquisition, Y.Y. and X.Z. All authors have read and agreed to the published version of the manuscript.

Funding: This study was supported by the Natural Science Foundation of Sichuan Province (Grant No. 22NSFSC3078) and the China Postdoctoral Science Foundation (Grant No. 2021M693909).

Data Availability Statement: Data available on request due to restrictions, e.g., privacy or ethical. The data presented in this study are available on request from the corresponding author. The data are not publicly available since the data in this study relate to the results of the project and are not readily available publicly.

Conflicts of Interest: Author Cancan Peng is employed by the company China National Petroleum Corporation Chuanqing Drilling Engineering Co., Ltd. Downhole Service Company. The remaining authors declare that the research was conducted in the absence of any commercial or financial relationships that could be construed as a potential conflict of interest.

References

1. Boswell, R.; Collett, T.S. Current Perspectives on Gas Hydrate Resources. *Energy Environ. Sci.* **2011**, *4*, 1206–1215. [[CrossRef](#)]
2. Wei, N.; Bai, R.-L.; Zhou, S.-W.; Luo, P.-Y.; Zhao, J.-Z.; Zhang, Y.; Xue, J. Development Strategy for Deep-sea Natural Gas Hydrates in China to Achieve Carbon Peak Goal. *Nat. Gas Ind.* **2022**, *42*, 156–165.
3. Torres, M.D.; Gadala-Maria, F.; Wilson, D.I. Comparison of the Rheology of Bubbly Liquids Prepared by Whisking Air into a Viscous Liquid (Honey) and a Shear-Thinning Liquid (Guar Gum Solutions). *J. Food Eng.* **2013**, *118*, 213–228. [[CrossRef](#)]
4. Li, Y.; Yu, Z. Distribution and Motion Characteristics of Bubbles in a Multiphase Rotodynamic Pump Based on Modified Non-Uniform Bubble Model. *J. Pet. Sci. Eng.* **2020**, *195*, 107569. [[CrossRef](#)]

5. Zhou, S.-W.; Chen, W.; Li, Q.-P. Green Mining Technology of Solid-state Fluidized Natural Gas Hydrates in Deep-water Shallow Layers. *China Offshore Oil Gas* **2014**, *26*, 1–7.
6. Zhang, D.; Shi, W.; (Bart) van Esch, B.P.M.; Shi, L.; Dubuisson, M. Numerical and Experimental Investigation of Tip Leakage Vortex Trajectory and Dynamics in an Axial Flow Pump. *Comput. Fluids* **2015**, *112*, 61–71. [[CrossRef](#)]
7. Sun, W.; Tan, L. Cavitation-Vortex-Pressure Fluctuation Interaction in a Centrifugal Pump Using Bubble Rotation Modified Cavitation Model Under Partial Load. *J. Fluids Eng. Trans. ASME* **2020**, *142*, 051206. [[CrossRef](#)]
8. Wang, C.; Zhang, Y.; Zhang, J.; Zhu, J. Flow Pattern Recognition inside a Rotodynamic Multiphase Pump via Developed Entropy Production Diagnostic Model. *J. Pet. Sci. Eng.* **2020**, *194*, 107467. [[CrossRef](#)]
9. Bosioc, A.I.; Tănasă, C. Experimental Study of Swirling Flow from Conical Diffusers Using the Water Jet Control Method. *Renew. Energy* **2020**, *152*, 385–398. [[CrossRef](#)]
10. Kadambi, J.R.; Charoengam, P.; Subramanian, A.; Wernet, M.P.; Sankovic, J.M.; Addie, G.; Courtwright, R. Investigations of Particle Velocities in a Slurry Pump Using PIV: Part 1, The Tongue and Adjacent Channel Flow. *J. Energy Resour. Technol.* **2004**, *126*, 271–278. [[CrossRef](#)]
11. Liu, Y.; Tan, L. Tip Clearance on Pressure Fluctuation Intensity and Vortex Characteristic of a Mixed Flow Pump as Turbine at Pump Mode. *Renew. Energy* **2018**, *129*, 606–615. [[CrossRef](#)]
12. Zhang, W.; Yu, Z.; Zhu, B. Influence of Tip Clearance on Pressure Fluctuation in Low Specific Speed Mixed-Flow Pump Passage. *Energies* **2017**, *10*, 148. [[CrossRef](#)]
13. Kan, K.; Yang, Z.; Lyu, P.; Zheng, Y.; Shen, L. Numerical Study of Turbulent Flow Past a Rotating Axial-Flow Pump Based on a Level-Set Immersed Boundary Method. *Renew. Energy* **2021**, *168*, 960–971. [[CrossRef](#)]
14. Kan, K.; Li, H.; Chen, H.; Xu, H.; Gong, Y.; Li, T.; Shen, L. Effects of Clearance and Operating Conditions on Tip Leakage Vortex-Induced Energy Loss in an Axial-Flow Pump Using Entropy Production Method. *J. Fluids Eng.* **2022**, *145*, 031201. [[CrossRef](#)]
15. Sonawat, A.; Kim, S.; Ma, S.-B.; Kim, S.-J.; Lee, J.B.; Yu, M.S.; Kim, J.-H. Investigation of Unsteady Pressure Fluctuations and Methods for Its Suppression for a Double Suction Centrifugal Pump. *Energy* **2022**, *252*, 124020. [[CrossRef](#)]
16. Lei, T.; Zhifeng, X.; Yabin, L.; Yue, H.; Yun, X. Influence of T-Shape Tip Clearance on Performance of a Mixed-Flow Pump. *Proc. Inst. Mech. Eng. Part A-J. Power Energy* **2018**, *232*, 386–396. [[CrossRef](#)]
17. Liu, M.; Tan, L.; Cao, S. Influence of Viscosity on Energy Performance and Flow Field of a Multiphase Pump. *Renew. Energy* **2020**, *162*, 1151–1160. [[CrossRef](#)]
18. Pablo Valdes, J.; Becerra, D.; Rozo, D.; Cediel, A.; Torres, F.; Asuaje, M.; Ratkovich, N. Comparative Analysis of an Electrical Submersible Pump's Performance Handling Viscous Newtonian and Non-Newtonian Fluids through Experimental and CFD Approaches. *J. Pet. Sci. Eng.* **2020**, *187*, 106749. [[CrossRef](#)]
19. Zhu, J.; Banjar, H.; Xia, Z.; Zhang, H.-Q. CFD Simulation and Experimental Study of Oil Viscosity Effect on Multi-Stage Electrical Submersible Pump (ESP) Performance. *J. Pet. Sci. Eng.* **2016**, *146*, 735–745. [[CrossRef](#)]
20. Ebrahimi, A.; Naranjani, B.; Milani, S.; Dadras Javan, F. Laminar Convective Heat Transfer of Shear-Thinning Liquids in Rectangular Channels with Longitudinal Vortex Generators. *Chem. Eng. Sci.* **2017**, *173*, 264–274. [[CrossRef](#)]
21. Li, W.-G. Mechanism for Onset of Sudden-Rising Head Effect in Centrifugal Pump When Handling Viscous Oils. *J. Fluids Eng.* **2014**, *136*, 074501. [[CrossRef](#)]
22. Amirafabi, M.; Khiadani, M.; Mohammed, H.A. Performance of a Dual Helical Ribbon Impeller in a Two-Phase (Gas-Liquid) Stirred Tank Reactor. *Chem. Eng. Process. Process. Intensif.* **2020**, *148*, 107811. [[CrossRef](#)]
23. Huang, T.; Li, C.; Jia, W.; Peng, Y. Application of Equations of State to Predict Methane Solubility under Hydrate-Liquid Water Two-Phase Equilibrium. *Fluid Phase Equilibria* **2016**, *427*, 35–45. [[CrossRef](#)]
24. Wei, R.; Shi, K.; Guo, X.; Wang, T.; Lv, X.; Li, Q.; Zhang, Y.; Zhao, J.; Yang, L. Evolving Thermal Conductivity upon Formation and Decomposition of Hydrate in Natural Marine Sediments. *Fuel* **2021**, *302*, 121141. [[CrossRef](#)]
25. Chen, B.; Sun, H.; Zhou, H.; Yang, M.; Wang, D. Effects of Pressure and Sea Water Flow on Natural Gas Hydrate Production Characteristics in Marine Sediment. *Appl. Energy* **2019**, *238*, 274–283. [[CrossRef](#)]
26. Liu, Z.; Song, Y.; Liu, W.; Liu, R.; Lang, C.; Li, Y. Rheology of Methane Hydrate Slurries Formed from Water-in-Oil Emulsion with Different Surfactants Concentrations. *Fuel* **2020**, *275*, 117961. [[CrossRef](#)]
27. Si, G. Experimentally Study the Rheology of Fine-Grained Slurries and Some Numerical Simulations of Downslopes Slurry Movements. Available online: <https://www.duo.uio.no/handle/10852/12443> (accessed on 28 July 2023).
28. Guo, X.; Stoesser, T.; Nian, T.; Jia, Y.; Liu, X. Effect of Pipeline Surface Roughness on Peak Impact Forces Caused by Hydrodynamic Submarine Mudflow. *Ocean Eng.* **2022**, *243*, 110184. [[CrossRef](#)]
29. Abdollahnejad, E.; Moghimi, M.; Derakhshan, S. Experimental and Numerical Investigation of Slip Factor Reduction in Centrifugal Slurry Pump. *J. Braz. Soc. Mech. Sci. Eng.* **2021**, *43*, 179. [[CrossRef](#)]
30. Wang, Z.; Ding, W.; Zhu, Z.; Liu, R.; Wang, C.; Yu, W.; Wang, Z. Experimental Study on Rheological Behaviors of Na-Bentonite Slurries under Seawater Intrusion. *Constr. Build. Mater.* **2022**, *357*, 129369. [[CrossRef](#)]
31. Deng, Y.; Wang, X.; Xu, J.; Li, Y.; Zhang, Y.; Kuang, C. Gas-Liquid Interaction Characteristics in a Multiphase Pump under Different Working Conditions. *Processes* **2022**, *10*, 1977. [[CrossRef](#)]
32. Xiao, Y.; Gui, Z.; Li, X.; Tao, S.; Shi, G.; Gu, C. Study on Distribution Law of Gas Phase and Cavitation in the Pressurization Unit of Helical Axial Flow Multiphase Pump. *J. Mar. Sci. Eng.* **2022**, *10*, 1795. [[CrossRef](#)]

33. Yu, Z.; Zhu, B.; Cao, S. Interphase Force Analysis for Air-Water Bubbly Flow in a Multiphase Rotodynamic Pump. *Eng. Comput.* **2015**, *32*, 2166–2180. [[CrossRef](#)]
34. Granados-Ortiz, F.-J.; Jimenez-Salas, M.; Ortega-Casanova, J. Application of Shear-Thinning and Shear-Thickening Fluids to Computational Fluid Mechanics of High-Reynolds Impinging Turbulent Jets for Cooling Engineering. *Int. J. Therm. Sci.* **2021**, *162*, 106753. [[CrossRef](#)]
35. Menter, F.R. Two-Equation Eddy-Viscosity Turbulence Models for Engineering Applications. *AIAA J.* **1994**, *32*, 1598–1605. [[CrossRef](#)]
36. Zhang, J.Y.; Zhu, H.W.; Ding, K.; Qiang, R. Study on Measures to Improve Gas-Liquid Phase Mixing in a Multiphase Pump Impeller under High Gas Void Fraction. *IOP Conf. Ser. Earth Environ. Sci.* **2012**, *15*, 062023. [[CrossRef](#)]
37. Menter, F.R. Review of the Shear-Stress Transport Turbulence Model Experience from an Industrial Perspective. *Int. J. Comput. Fluid Dyn.* **2009**, *23*, 305–316. [[CrossRef](#)]
38. Sun, H.; Luo, Y.; Yuan, S.; Yin, J. Hilbert spectrum analysis of unsteady characteristics in centrifugal pump operation under cavitation status. *Ann. Nucl. Energy* **2018**, *114*, 607–615. [[CrossRef](#)]
39. Sun, W.; Yu, Z.; Zhang, K.; Zhang, W. Effect of Shear-Thinning Property on Vortex Evolution and Pressure Fluctuation in an Axial Flow Pump. *Chem. Eng. Commun.* **2023**, *211*, 192–204. [[CrossRef](#)]

Disclaimer/Publisher’s Note: The statements, opinions and data contained in all publications are solely those of the individual author(s) and contributor(s) and not of MDPI and/or the editor(s). MDPI and/or the editor(s) disclaim responsibility for any injury to people or property resulting from any ideas, methods, instructions or products referred to in the content.